iScience

Article

Primitive to visceral endoderm maturation is essential for mouse epiblast survival beyond implantation

Graphical abstract

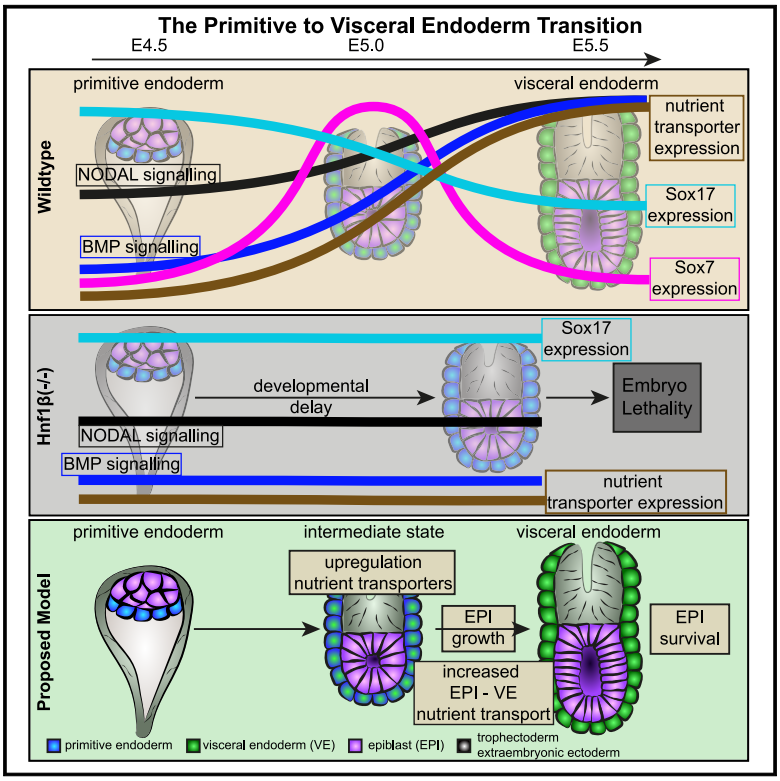

Highlights

- The primitive to visceral endoderm maturation displays dynamic signaling activities
- E5.0 exhibits primitive and visceral endoderm transcriptomes at intermediate levels
- Hnf1b KO lethality suggests the crucial interaction of epiblast and visceral endoderm

Authors

Antonia Weberling, Dylan Siriwardena, Christopher Penfold, Neophytos Christodoulou, Thorsten E. Boroviak, Magdalena Zernicka-Goetz

Correspondence

mz205@cam.ac.uk

In brief

Biological sciences; Cell biology; Developmental biology; Embryology; Natural sciences

Weberling et al., 2025, iScience *28*, 111671
January 17, 2025
https://doi.org/10.1016/j.isci.2024.111671

CellPress

iScience

CellPress
OPEN ACCESS

Article

Primitive to visceral endoderm maturation is essential for mouse epiblast survival beyond implantation

Antonia Weberling,[1,6,7] Dylan Siriwardena,[2,3,4] Christopher Penfold,[2,3,4] Neophytos Christodoulou,[1,8] Thorsten E. Boroviak,[2,3,4] and Magdalena Zernicka-Goetz[1,5,9,*]

[1]Mammalian Embryo and Stem Cell Group, University of Cambridge, Department of Physiology, Development and Neuroscience, Downing Street, Cambridge CB2 3DY, UK

[2]Department of Physiology, Development and Neuroscience, University of Cambridge, Downing Site, Cambridge CB2 3EG, UK

[3]Centre for Trophoblast Research, University of Cambridge, Downing Site, Cambridge CB2 3EG, UK

[4]Wellcome Trust - Medical Research Council Stem Cell Institute, University of Cambridge, Jeffrey Cheah Biomedical Centre, Puddicombe Way, Cambridge CB2 0AW, UK

[5]Plasticity and Self-Organization Group, California Institute of Technology, Division of Biology and Biological Engineering, 1200 E. California Boulevard, Pasadena, CA 91125, USA

[6]Present address: All Souls College, University of Oxford, Oxford OX1 4AL, United Kingdom

[7]Present address: Nuffield Department of Women's' and Reproductive Health, University of Oxford, Women's Center (Level 3), John Radcliffe Hospital OX3 9DU, United Kingdom

[8]Present address: Department of Biological Sciences, University of Cyprus, 2109, Nicosia, Cyprus

[9]Lead contact

*Correspondence: mz205@cam.ac.uk

https://doi.org/10.1016/j.isci.2024.111671

SUMMARY

The implantation of the mouse blastocyst initiates a complex sequence of tissue remodeling and cell differentiation events required for morphogenesis, during which the extraembryonic primitive endoderm transitions into the visceral endoderm. Through single-cell RNA sequencing of embryos at embryonic day 5.0, shortly after implantation, we reveal that this transition is driven by dynamic signaling activities, notably the upregulation of BMP signaling and a transient increase in Sox7 expression. Embryos deficient in Hepatocyte nuclear factor-1-beta (Hnf1b−/−), a gene critical for visceral endoderm differentiation, showed an interaction between visceral endoderm and epiblast, crucial for epiblast survival. Single-cell RNA profiling of Hnf1b−/− visceral endoderm shows developmental delays and severe dysregulation in several nutrient transport pathways. Impaired glucose uptake in Hnf1b−/− embryos suggests that the activation of nutrient transport mechanisms during the primitive-to-visceral endoderm transition may be vital for post-implantation epiblast development. These findings offer new insights into the molecular regulation of early mammalian development.

INTRODUCTION

During implantation, the mammalian embryo undergoes dramatic transcriptional and morphogenetic changes.[1,2] Immediately prior to implantation, at embryonic day (E) 4.5, the mouse blastocyst consists of embryonic epiblast (EPI), surrounded by extraembryonic trophectoderm (TE) and primitive endoderm (PE). The TE overlies the proximal side of the EPI with its polar side, while the mural side forms the blastocoelic cavity. In contrast, the PE envelops the distal portion of the EPI toward the blastocoelic cavity.[3–6] Implantation is mediated by the mural TE, which differentiates into trophoblast giant cells. The polar TE retains multipotency and develops into the extraembryonic ectoderm, a multi-layered pseudostratified epithelium that invaginates and pushes the EPI into its characteristic cylindrical shape.[7,8] Concurrently, the EPI transforms from a group of non-polar cells into a polarized mono-layered epithelium surrounding a central lumen.[9–13] These morphological changes mark the transition from naive to formative and ultimately primed pluripotency in the EPI. Simultaneously, PE expands and differentiates into the visceral endoderm (VE), which covers both the EPI and extraembryonic ectoderm by E5.0.[8] As development progresses, a subset of VE cells located at the distal tip of the egg cylinder specify into the distal visceral endoderm (DVE) and migrate toward one side of the embryo, where they ultimately form the anterior visceral endoderm (AVE).[14] This migration regulates the formation of the anterior-posterior axis through the secretion of Nodal, Tgfβ, and Wnt inhibitors by the AVE, which confines primitive streak formation toward the opposite (posterior) side of the EPI.[15–18] This highlights the important role of signaling at the interface of embryonic and extraembryonic lineages for successful post-implantation development.

PE specification and the role of the AVE during anterior-posterior patterning have been studied in detail,[16,18–22] however, the molecular machinery driving the transition from PE to VE remains poorly understood. Previous studies suggest that loss of Hepatocyte Nuclear Factor 1 beta (*Hnf1b*) results in failure of VE specification, egg cylinder formation and eventually embryo lethality

at E5.5–6.5.[23,24] Hnf1b is a transcription factor that interacts directly with the PE lineage driver *Gata6* to induce the expression of *Hnf4a* in the VE.[25] Loss of Hnf4a results in embryo lethality at E7.5–8.5.[25,26] While the role of Hnf1b in epithelial maturation during organogenesis of kidney, liver and intestine has been explored,[25] the mechanisms by which Hnf1b regulates embryo survival during peri-implantation development remain unknown.

Here, we identify a direct interaction based on nutrient transport pathways between the EPI and the VE lineages that is required for EPI survival soon after implantation. Our results indicate that failure of the PE to VE differentiation leads to a deficiency in glucose uptake in the VE and dysregulation of nutrient transporters, which points toward a requirement of PE to VE differentiation for EPI proliferation and survival beyond implantation.

RESULTS

Dynamic molecular changes on the transcriptome and protein level during the primitive to visceral endoderm transition

In order to examine the molecular signature of the PE to VE transition (Figure 1A), we performed single-cell RNA sequencing (scRNAseq) of E5.0 mouse embryos, a time point that has not been assessed in previously published studies that focus on the early post implantation development.[27,28] We collected 48 cells from mouse embryos and integrated our data with a published mouse embryo scRNAseq dataset[27] spanning from late blastocyst (E4.5) to the gastrulating egg cylinder (E6.5) (Figures 1A–1C, S1A, and Table S1). Lineage identity was determined by the expression of specific lineage marker genes and unbiased clustering. We found that VE at E5.0 clustered in-between the E4.5 PE and E5.5 VE (Figure 1B, cluster 1), consistent with developmental progression and shared common PE and VE marker expression (Figure 1C). To ensure these differences were not solely due to batch effects, we performed diffusion pseudo-time and principal component analysis, which both localized the E5.0 VE in-between E4.5 and E5.5, suggesting E5.0 VE to be an intermediate state between PE and VE (Figures 1C, S1B, and S1C). To elucidate the gene expression dynamics of the developing PE lineage during this time, we conducted a pairwise differential expression analysis between E4.5 and E5.0 (250 significantly differentially expressed genes) and E5.0 and E5.5 (85 significantly differentially expressed genes) (Figures 1D, 1E and Table S2). We observed a continuous downregulation of PE marker genes such as *Pdgfra*, *Sox17*, *Sox7* as well as several extracellular matrix components from E4.5 to E5.5, including *Lama1*, *Lamb1*, *Col4a1/2*, with E5.0 presenting an intermediate time point (Figures 1D and 1E). Simultaneously, differentiation markers such as *Otx2, Ttr, Apoa1*, *Apob, and Cerl1* became steadily upregulated (Figures 1D and 1E). To gain further insight into the progression from PE to VE differentiation, we analyzed the expression levels of *Gata4*, *Gata6*, *Sox7*, *Sox17*, *Pdgfra*, *Otx2*, *Lefty1*, *Cer1*, *Ttr*, and *Hhex* in more detail. We found that E5.0 embryos exhibited intermediate expression of PE marker genes such as *Pdgfra*, *Sox17* and *Sox7* as well as of VE markers such as *Otx2* and *Ttr*, supporting E5.0 as a transitional time point (Figures S2A–S2J).

To understand whether the above transcriptional changes were also reflected on the protein level, we performed immunostaining for Gata4, Sox7, Sox17, Otx2, Lefty1 and Cer1. Gata4 exhibited high expression at each time point (Figure S2A). Interestingly, at a protein level, we could not detect Sox7 expression at E4.5 but found it highly expressed at E5.0 before being downregulated again at E5.5 (Figures 1F and S2B). Sox17 protein became downregulated at E5.0 and then showed upregulation in the extraembryonic visceral endoderm at E5.5 (Figures 1F and S2C), which deviates from their respective transcription levels. Embryonic VE marker Otx2 became upregulated on the protein level at E5.0 and then exhibited even higher expression at E5.5 (Figures 1F and S1D). DVE and AVE marker Lefty1 could be detected at E5.5 (Figure S2E), while Cer1 could not be detected (Figure S2F). Due to basement membrane components becoming downregulated over time, we assessed the expression of *Lama1*, *Lamb1*, and *Lamc1* in all lineages in more detail at a transcriptomic level (Figures S3A–S3C), and Lama1 at a protein level at E4.5/5.0/5.5 (Figure S3D). Interestingly, at E4.5 Lama1 was highly expressed and localized peri-cellularly, while at E5.0 it was resolved into a thin layer of basement membrane that exhibited several large perforations at the tip of the EPI, as reported before.[7,29] At E5.5, Lama1 was again more abundantly expressed in the VE, exhibiting small perforations across the EPI,[29] which deviates from the transcriptome data pointing toward an additional level of protein expression control. Taken together, our results suggest a continuous transition of the PE to VE with E5.0 as an intermediate time point at which we could detect a transient upregulation of Sox7 and downregulation of Sox17 and Lama 1 at E5.0 on the protein level.

Signaling changes during the primitive to visceral endoderm transition

In order to identify key signaling cascades that may promote PE to VE maturation, we examined the enrichment of developmentally relevant signaling pathways from E4.5 to E6.5 (Figure 2A). We found that TGFβ and WNT signaling pathway enrichment scores were increased upon implantation at E5.0, whereas expression of genes associated with PI3K/AKT, HIPPO, JAK/STAT and mTOR signaling decreased compared to E4.5 PE. The Fgf/Mapk signaling pathway showed scattered enrichment across time. TGFβ signaling pathway components, including *Nodal*, *Bmp2*, *Pitx2* and *Smad1* were upregulated (Figures 2B and S4A). To determine signaling pathway activity at the protein level, we analyzed the nuclear localization of protein read-outs for the Bmp and Nodal pathways by analysing the nuclear to cytoplasmic ratio of Smad2/3 and normalized nuclear phosphorylated (p) Smad1/5 at three developmental stages. Smad2/3 was highly expressed in E4.5 PE with nuclear localization increasing further toward E5.0 and E5.5 (Figures 2C and 2D). pSmad1/5 could not be detected at E4.5, but then became strongly activated at E5.0 in a subset of embryos (Figures 2E, 2F, S5A, and S5B). At E5.5, distal VE cells became negative for pSmad1/5 whereas all other cells retained high levels of nuclear pSmad1/5 in line with a previous study.[30] For FGF signaling, we could instead observe the downregulation of *Fgfr2* and *Pdgfra*, while expression of *Fgf5* and *Fgf8* increased (Figures S6A and S6B). We stained for pERK at E4.5/5/0/5/5 (Figure S6C) and recorded a fraction of embryos exhibiting normalized nuclear pERK at E4.5 and a slight but significant upregulation at E5.0 in a subset of embryos with embryos exhibiting

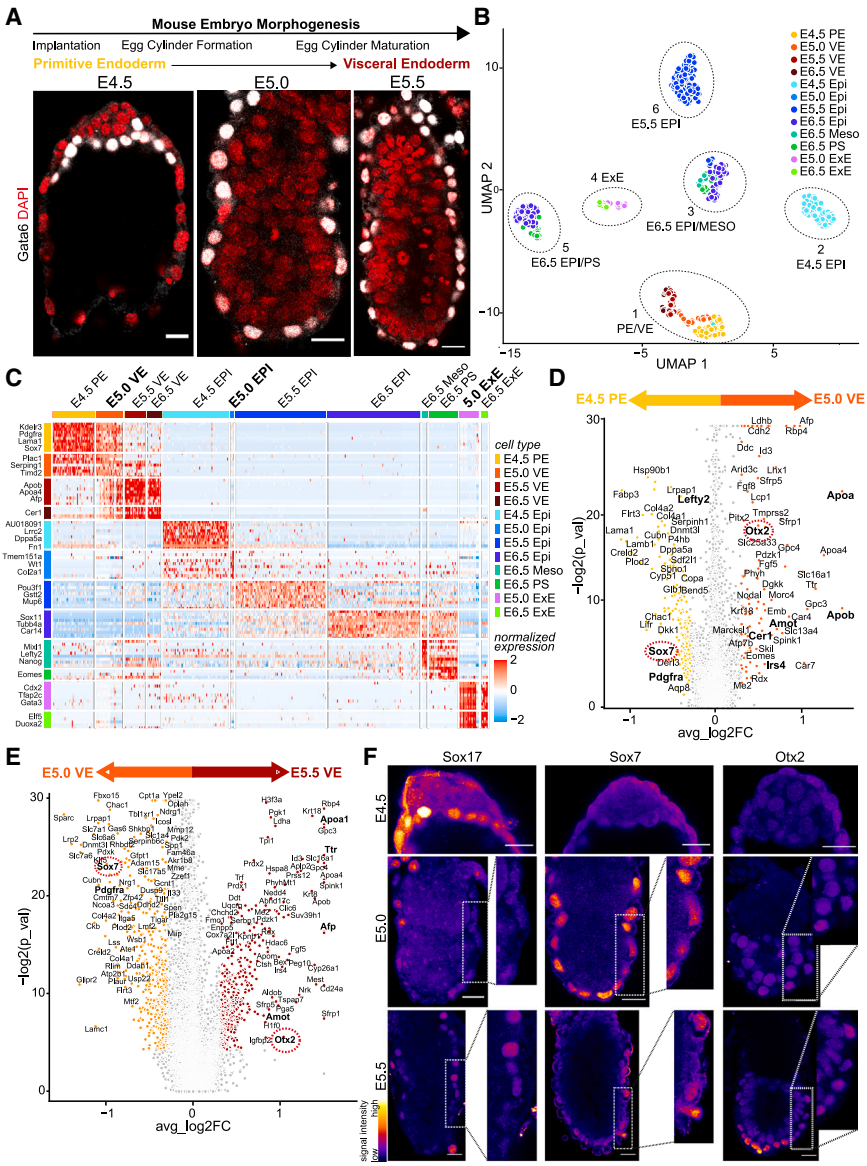

Figure 1. Primitive endoderm differentiates via an intermediate state into the visceral endoderm

(A) Representative examples of mouse embryos at E4.5/5.5/6.5. Gata6 (white), DAPI (red).

(B) UMAP of mouse developmental trajectory from E4.5 to E6.5. E5.0 single cell RNA sequencing dataset was integrated with.[27] Cluster labels were determined by gene expression. PE, primitive endoderm; VE, Visceral endoderm; EPI, Epiblast; MESO, mesoderm; PS, primitive streak; ExE, extraembryonic ectoderm.

(C) Heat gene of unbiased lineage marker expression in mouse developmental trajectory. Relative mRNA were scaled across samples. Full list of genes assessed in Table S1. Red: high expression, blue: downregulation.

(D and E) Volcano plot of differentially expressed genes between E4.5 primitive endoderm and E5.0 visceral endoderm (D) or E5.0 visceral endoderm and E5.5 visceral endoderm (E). Full list of differentially expressed genes found in Table S2.

(F) Immunofluorescence staining of PE/VE marker genes Sox17 (left), Sox7 (middle), Otx2 (right) at E4.5 (top row), E5.0 (middle row), E5.5 (bottom row). Fire intensity staining, color bar included. Representative of 8 embryos. All scale bars 20 μm.

fully nuclear pERK or none (Figures S6D–S6F). At E5.5, pERK was mostly absent in the VE (Figures S6C and S6G).

Together, these results indicate that Fgf signaling may become transiently upregulated during the PE to VE transition, while Nodal signaling is active already at E4.5 and then increases its activity during the differentiation of the PE. Bmp signaling becomes upregulated throughout the VE tissue upon reaching E5.0. This expression pattern suggests that E5.0 presents a switch point in Bmp and Nodal signaling.

Loss of hepatocyte nuclear factor-1-beta results in defective morphogenesis

To understand the role of the PE to VE differentiation for embryogenesis, we decided to focus on Hnf1b. Hnf1b has been reported to be an essential regulator of PE to VE maturation with its loss being lethal at E5.5.[23,24] We therefore decided to determine the expression of its direct downstream target, the VE-specific transcription factor Hnf4a, which could be used as proxy for Hnf1b activity.[25] We found that *Hnf4a* was progressively upregulated in the PE/VE between E4.5 and E6.5 (Figure 3A). Despite being expressed at low levels on the mRNA level at E4.5, we were able to detect Hnf4a protein only from E4.75 onwards, corresponding with progression from PE to VE presenting it as a novel marker for the PE to VE differentiation (Figure 3B).[23]

We next wished to examine the phenotype of *Hnf1b*$^{-/-}$ embryos at this transitional peri-implantation period, we first determined that, as a direct downstream target, Hnf4a protein levels correspond with knock out of *Hnf1b*. To this end, we recovered embryos at E5.5 and confirmed that *Hnf1b*$^{+/+}$ and *Hnf1b*$^{+/-}$ embryos were morphologically indistinguishable, exhibiting Hnf4a expression in all VE cells (Figure 3C first two columns, 3D). We therefore combined *Hnf1b*$^{+/+}$ and *Hnf1b*$^{+/-}$ embryos in all future analyses. In contrast, the *Hnf1b*$^{-/-}$ mutant embryos did not form egg cylinders, were significantly smaller, and did not express Hnf4a (Figures 3C and 3D). As the *Hnf1b*$^{-/-}$ embryos were degenerated by E5.5, we recovered embryos at E5.0, when wildtype embryos had just completed the blastocyst to egg cylinder transition (Figure 3E, top row). In contrast, *Hnf1b*$^{-/-}$ embryos were arrested (Figure 3E, bottom row). The polar TE in mutant embryos formed a double layer and exhibited increased actin intensity but failed to fold in, as would normally happen in wildtype embryos.[7,8] This could be

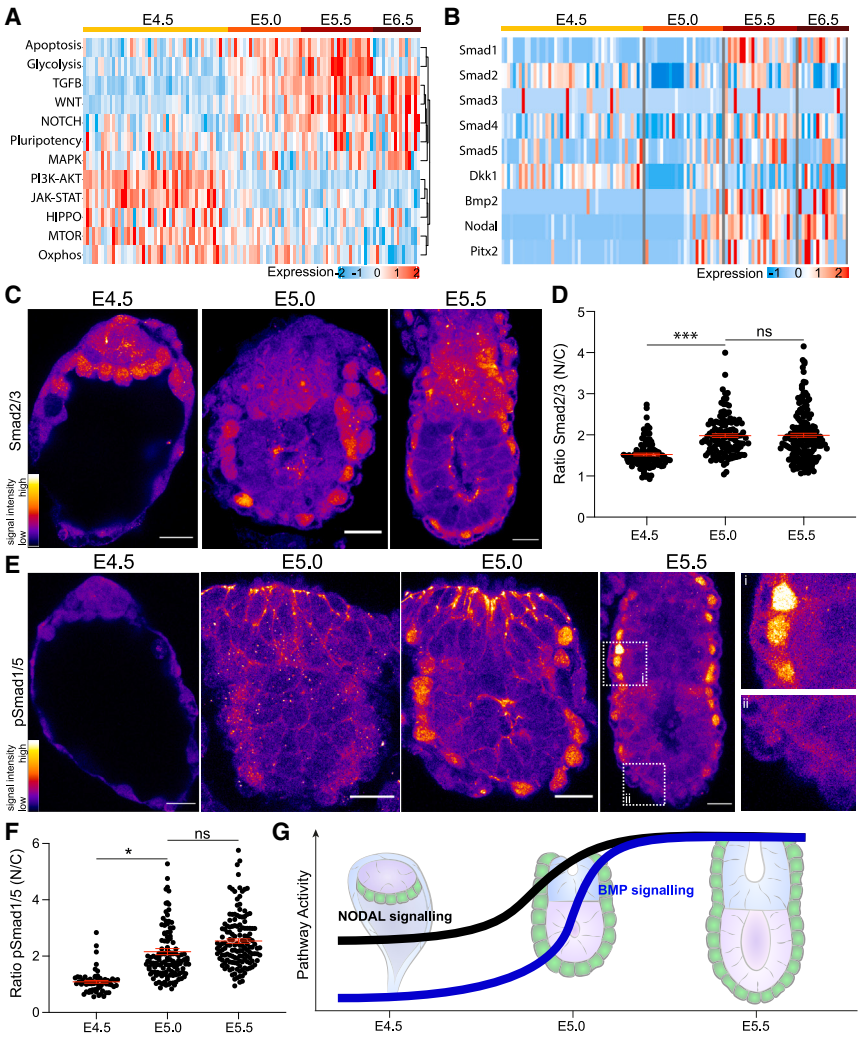

Figure 2. Common signaling pathways exhibit dynamic activity during the primitive to visceral endoderm differentiation

(A) Heatmap of KEGG pathway enrichment from E4.5-E6.5 primitive/visceral endoderm.

(B) Heatmap of normalized mRNA expression levels of known TGFB signaling components from E4.5-E6.4 in the primitive/visceral endoderm. Full list in Figure S4A. (B/C) red: high expression, blue: downregulation. (C and D) Analysis of Nodal signaling activity in the primitive/visceral endoderm.

(C) Stainings of E4.5/E5.0/E5.5 total Smad2/3.

(D) Quantitative analysis of the nuclear to cytoplasmic ratio of Smad2/3. Scatterplot, mean ± SEM, E4.5 $n = 13$, E5.0 $n = 13$, E5.5 $n = 10$ embryos, Analysis: nested t-test. E4.5-E5.0: $p = 0.0009$, E5.0-E5.5: $p = 0.9204$. 1-way Anova: $p = 0.0027$.

(E and F) Analysis of canonical Bmp signaling activity in the primitive/visceral endoderm. (E) Stainings of E4.5/E5.0/E5.5 pSmad1/5. (F) Quantitative analysis of the normalized nuclear expression of pSmad1/5. Scatterplot, mean ± SEM, E4.5 $n = 11$, E5.0 $n = 18$, E5.5 $n = 9$ embryos, Analysis: nested t-test. E4.5-E5.0: $p = 0.0132$, E5.0-E5.5: $p = 0.6341$.1-way Anova: $p = 0.0063$. g. Schematic of signaling activity from E4.5 to E5.5. Fire staining to represent intensity, color bar included in figure. All Scale bars 20 μm.

due to a developmental delay or failure of the folding process. Considering that loss of Hnf1b results in defective epithelization during ureteric bud branching,[31] we wished to examine VE epithelialization in *Hnf1b* mutants. To this end, we assessed the adherens junctional marker E-Cadherin in *Hnf1b*$^{-/-}$ and control embryos and found that lateral E-Cadherin levels were lower in *Hnf1b*$^{-/-}$ compared to controls (Figures 3F–3K). The formation of a polarized epithelium in the VE requires basolateral Integrin (Itgb1) localization, confining F-actin toward the EPI surface (Figure 4A). *Hnf1b*$^{-/-}$ embryos expressed Itgb1 basolaterally and exhibited high F-Actin intensity at the apical surface of the cells similar to control embryos (Figure 4B). Both control and *Hnf1b*$^{-/-}$ embryos had Itgb1 sorted to the basal side of the PE/VE cells. However, control embryos showed significantly higher levels of relative intensity (Figures 4C and S7A). To understand whether these lower levels of E-Cadherin and Itgb1 affect PE/VE apicobasal polarity, we examined the localization of Podocalyxin (Podxl), an apically secreted protein important for lumenogenesis,[13] at E5.0. In control embryos, Podxl localized to the apical surface of the VE similarly to *Hnf1b*$^{-/-}$ embryos (Figures 4D–4F). To quantify Podxl, we assessed the ratio of apical to basal intensity in control and Hnf1b$^{-/-}$ embryos. Both exhibited high Podxl levels at the apical surface, though *Hnf1b*$^{-/-}$ embryos showed lower levels. Considering the appropriate localization of E-Cadherin, Integrin and Podocalyxin, we conclude that Hnf1b is not required for epithelial integrity in VE during egg-cylinder formation at E5.0.

We noted that the EPI was significantly smaller in *Hnf1b*$^{-/-}$ embryos (Figures 3C and 3E), which suggested a developmental delay in Hnf1b$^{-/-}$ mutants. Consequently, we assessed EPI morphology. Polarization and epithelialization were comparable between controls and *Hnf1b*$^{-/-}$ embryos (Figure 4G). To examine developmental progression, we analyzed naïve-to-primed pluripotency markers Nanog, Otx2[32] and the Golgi protein and apical marker GM130. Control and *Hnf1b*$^{-/-}$ embryos showed the upregulation of Otx2 and downregulation of Nanog in the EPI at E5.0 (Figures 4H and S7B), indicative of successful exit from naive pluripotency.[33] The GM130 enrichment at the apical side confirmed the EPI polarization of *Hnf1b*$^{-/-}$ embryos. Together, these results suggest that *Hnf1b*$^{-/-}$ lethality is not due to an inability of the EPI to mature during post-implantation development.

Hepatocyte nuclear factor-1-beta mediates a direct signaling interaction required for epiblast growth and survival

To track the events leading up to embryonic lethality in *Hnf1b*$^{-/-}$ embryos in real time, we introduced an endogenous homozygous

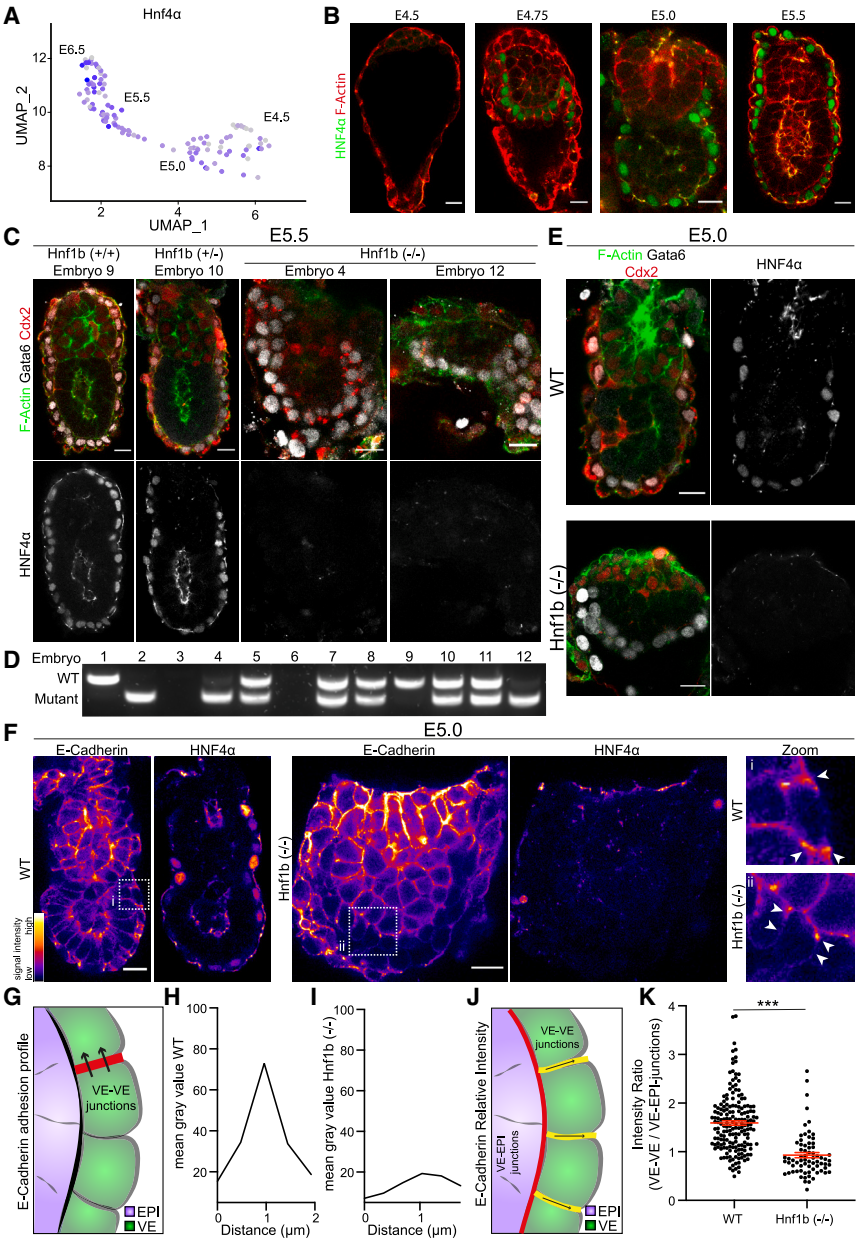

Figure 3. Loss of HNF1B results in embryo lethality following implantation

(A) UMAP of normalized *Hnf4a* mRNA levels in the primitive/visceral endoderm. Point darkness represents gene expression.

(B) Stainings of Hnf4a at consecutive timepoints E4.5/E4.75/E5.0/E5.5. green: Hnf4a, red: F-Actin.

(C and D) Staining and genotyping of E5.5 embryos from Hnf1b HETxHET cross.

(C) Upper row: green: F-Actin, red: Cdx2, white: Gata6, bottom row: white: Hnf4a. Embryo labeled according to genotype assessment in (D).

(E) Staining of E5.0 HNF1B mutant embryos, top row: WT, bottom row: KO, left column: F-Actin green, Gata6 white, Cdx2 red; right column: Hnf4a white.

(F–K) Assessment of adherens junctions in Hnf1b WT versus KO at E5.0.

(F) Staining of WT and mutant embryos for E-Cadherin and Hnf4a. Fire intensity staining, color bar included.

(G) Schematic of plot profile assessment in Figure (H/I).

(H) Intensity profile of single adherens junction in WT.

(I) Intensity profile of single adherens junction in KO.

(J) Schematic of the relative intensity measurement of E-Cadherin in WT versus KO embryos in (K).

(K) Quantitative analysis of relative E-Cadherin intensity in visceral endoderm (VE-VE junctions were normalized against VE-EPI junctions. Scatterplot, mean ± SEM, WT $n = 17$, KO $n = 9$ embryos, Analysis: nested t-test. WT-KO: $p = 0.0007$. All Scale bars 20 μm.

E-Cadherin-GFP into the *Hnf1b*$^{-/-}$ mouse line and performed live imaging from E4.85 (Figure 5A, Videos S1 and S2). Control embryos successfully developed into egg cylinders covered by Hnf4a-positive VE. *Hnf1b*$^{-/-}$ embryos were initially able to form egg cylinders such as control embryos, but then failed to grow and expand as control embryos did but degenerated instead, which explains the lack of egg cylinders recovered at E5.0 (Figures 5A and 5B). To examine whether apoptosis plays a role in the *Hnf1b*$^{-/-}$ phenotype, we performed live imaging of cleaved-Caspase3 expression (cCasp3). Control embryos showed few cCasp3-positive cells. cCasp3 levels increased after 14h of imaging, which was likely due to phototoxicity (Figure 5C). The extraembryonic ectoderm (ExE) of *Hnf1b*$^{-/-}$ embryos similarly invaginated to form egg cylinders and did not exhibit high levels of cCasp3 until after 14h of imaging, after which the entire embryo became cCasp3 positive to levels similar to control embryos (Figures 5D, 5E, S8A, S8B, Videos S3, S4, S5, S6, S7, and S8). However, *Hnf1b*$^{-/-}$ embryos did not grow over time and remained the same size. Measuring embryo length in control versus *Hnf1b*$^{-/-}$ embryos consistently showed that mutant embryos were significantly smaller (Figures 5F and S8C). To determine whether this decrease in EPI growth was due to a direct interaction between EPI and VE or through an indirect effect, potentially mediated by the ExE, we removed the TE by immunosurgery at the blastocyst stage and cultured the remaining embryos *in vitro*. After 48h of embryo culture, *Hnf1b*$^{-/-}$ EPIs were significantly smaller (Figures 5G, 5H, and S8D), suggesting that Hnf1b-mediated lineage progression from PE into VE is required for EPI growth (Figure 5I).

To determine the possible factors that contribute to EPI lethality in the absence of Hnf1b, we performed scRNAseq of *Hnf1b*$^{-/-}$ embryos at E5.0. Integrated analysis with the wildtype dataset showed that *Hnf1b*$^{-/-}$ mutant cells clustered

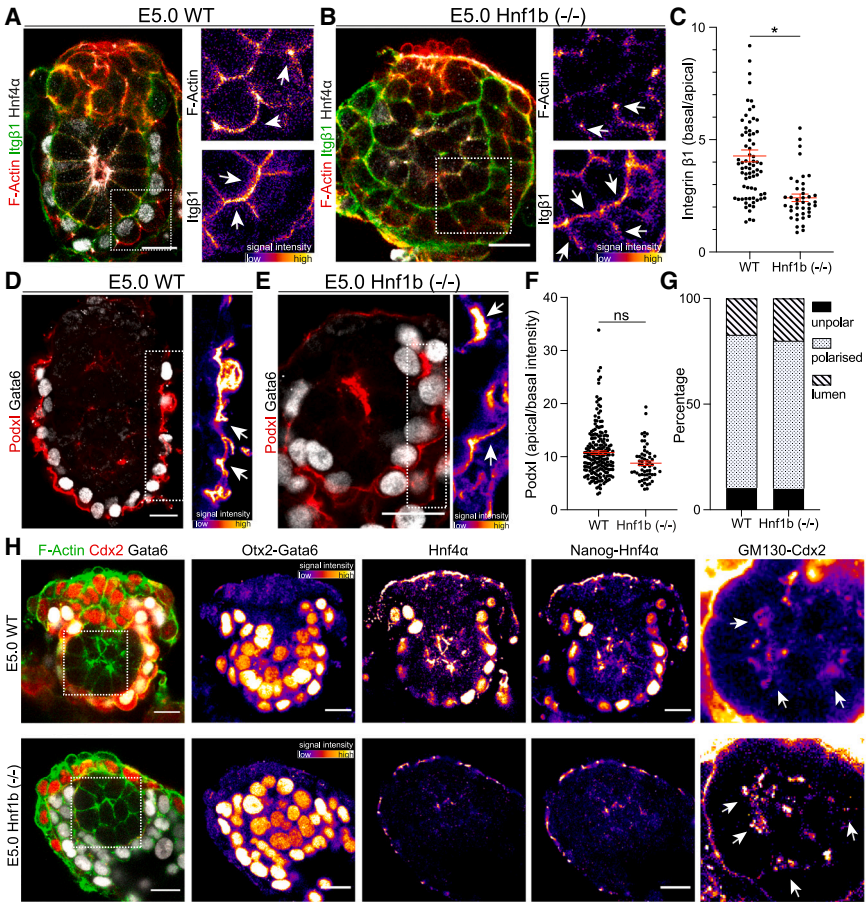

Figure 4. HNF1B deficiency does not affect epiblast morphogenesis

(A and B) Staining of E5.0 WT (A) and KO (B) embryos for F-Actin (red), ItgB1 (green), Hnf4a (white). Fire Intensity staining to reflect intensity, color bar provided.

(C) Quantitative analysis of relative integrin intensity (basal/apical). Scatterplot, mean ± SEM, WT n = 19, KO n = 5 embryos, Analysis: nested t-test. WT-KO: p = 0.0210. Schematic for analysis provided in Figure S7A.

(D and E) Staining of PodxI (red) and Gata6 (white) in WT (D) versus KO (E) E5.0 embryos.

(F) Quantitative analysis of apical/basal PodxI intensity. Scatterplot, mean ± SEM, WT n = 20, KO n = 9 embryos, Analysis: nested t-test. WT-KO: p = 0.0873. Schematic for analysis provided in Figure S7A.

(G) Assessment of epiblast morphogenesis at E5.0 WT vs. KO, WT n = 29, KO n = 10 embryos.

(H) Staining of epiblast differentiation in WT (top row) versus KO (bottom row). F-Actin (green), Cdx2 (red), Gata6 (white), staining pattern in Figure S7B. All Scale bars 20 μm.

away from E5.0 wildtype VE and, instead, localized toward the PE cluster (Figures 6A and S9A). Diffusion pseudo-time and correlation analysis showed the *Hnf1b*$^{-/-}$ VE indeed clustered closest to the E4.5 PE (Figures S9B–S9D). We examined the differentially expressed genes between E5.0 *Hnf1b*$^{-/-}$ and E4.5/E5.0/E5.5 PE/VE WT, focusing on PE/VE marker genes (*Fzd5/Pdgfra/Hnf4a/Dkk1/Otx2/Hnf1b/Cer1/Nodal/Hhex/Ttr/Lhx1/Gsc/Afp/Lefty2/Gata6/Sox7/Lefty1/Gata4*) (Table S3 and Figures S10A–S10R). These data demonstrate that PE to VE differentiation is defective in the absence of Hnf1b at the transcriptome level. Further analysis of the differentially expressed genes revealed a strong upregulation of basement membrane components in *Hnf1b*$^{-/-}$ compared to WT embryos (Figures 6B and S11A–S11D and Table S3). Analyses of the basement membrane components Lama1 and Collagen IV showed that despite appearing thickened compared to WT embryos, the basement membrane of *Hnf1b*$^{-/-}$ exhibited a similar intensity pattern over the length of the EPI compared to controls (Figures 6C–6F).

When examining expression of transcription factors, we identified the upregulation of *Sox17* and *Oct4* in the *Hnf1b*$^{-/-}$ versus the WT PE/VE (Figures S11E, S11F, and Table S3). To understand whether this upregulation was also present at the protein level, we stained for Sox17 and Oct4 at E5.0. Control embryos showed sporadic expression of Sox17 in the extra-embryonic portion of the VE as shown previously.[34] However, *Hnf1b*$^{-/-}$ embryos exhibited Sox17 expression in every single cell of the PE/VE, similar to the expression pattern in E4.5 PE (Figures 6G and 6H). Oct4 expression was confined to the EPI lineage in WT but expressed in the PE/VE of KO embryos (Figures 6G and 6I). These data suggest that the loss of Hnf1b does not only delay VE development but induces other aberrant gene expression patterns.

Upregulation of nutrient exchange pathways is crucial to primitive endoderm maturation and epiblast survival

We next wished to examine how the loss of Hnf1b perturbs the signaling landscape during peri-implantation development. To this end, we determined the enrichment of developmentally relevant signaling cascades in *Hnf1b*$^{-/-}$ embryos, as previously done for WT embryos (Figure 7A). We found that pluripotency factors, mTOR, TGFβ, MAPK, WNT, and PI3K-AKT signaling appeared similar to WT. As previously noted, Nodal, Fgf, and Bmp signaling showed dynamic activity during the PE to VE transition. To test whether these signaling activities were affected, we assessed the protein localization and/or phosphorylation for markers of all three pathways (Figures 7B, 7C, and S12A). We found that E5.0 KO embryos exhibited lower signaling activity for Nodal, Fgf, and Bmp than E5.0 controls, coinciding with their failure to differentiate. Interestingly, the Glycolysis module score, which showed a profound upregulation at E5.0 in WT (Figure 2A), exhibited decreased activity levels comparable to E4.5 for the E5.0 KO (Figure 7A).

Hnf1b is known as a key factor in regulating nutrient transport in the kidney, intestines, and liver.[35–37] Additionally, a recent study

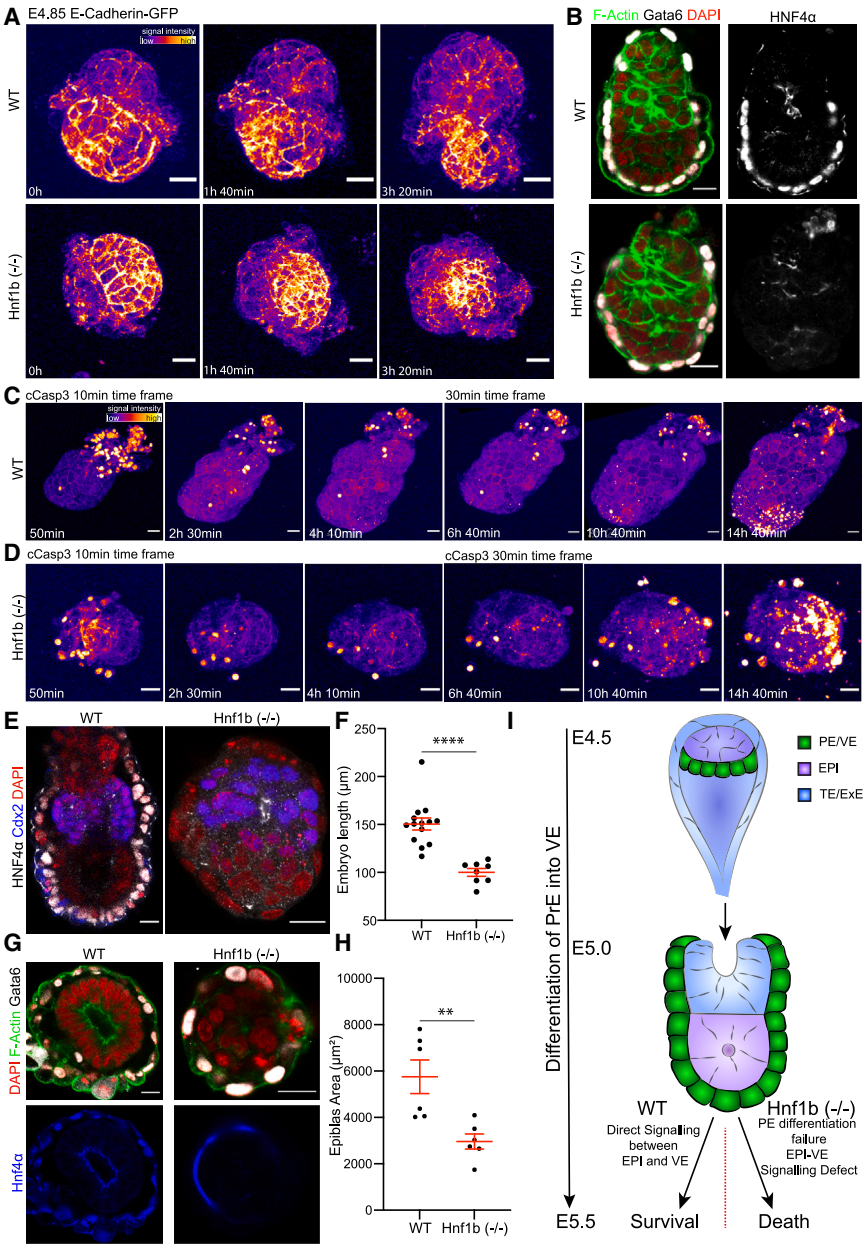

Figure 5. Epiblast lethality in Hnf1b deficient embryos due to direct signaling interaction between primitive/visceral endoderm and epiblast

(A) Stills from time lapse movie of E-Cadherin-GFP homozygous Hnf1b WT (top row) versus KO (bottom row) E4.85 embryos. Video S1 and S2. Fire staining to reflect intensity, color bar included.

(B) Staining of imaged embryos (A). Top row WT, bottom row KO. left column: F-Actin (green), Gata6 (white), DAPI (red); right column: Hnf4a white.

(C and D) Stills from time lapse imaging of E-Cadherin-GFP homozygous Hnf1b WT (C) versus KO (D) E4.85 embryos using cleaved-Caspase3 live dye. Videos S3, S4, S5, and S6.

(E) Staining of imaged embryos (C/D). Hnf4a (white), Cdx2 (blue), DAPI (red).

(F) Quantitative analysis of total embryo length (Figure S5C). Scatterplot, mean ± SEM, WT $n = 14$, KO $n = 8$ embryos, Analysis: unpaired t-test. WT-KO: $p < 0.0001$.

(G) Staining of Immunosurgery of E4.5 Hnf1b mutant embryos cultured for 48h in hanging drops. Left column (WT), right column (KO). top row: DAPI (red), F-Actin (green), Gata6 (white); bottom row: Hnf1a (blue).

(H) Quantitative analysis of maximal epiblast area (Figure S5D) of WT versus KO structures (G). Scatterplot, mean ± SEM, WT $n = 6$, KO $n = 6$ embryos, Analysis: unpaired t-test WT-KO p-value = 0.0057.

(I) Model of role of primitive to visceral endoderm differentiation mediated by Hnf1b. All Scale bars 20 μm.

highlighted the changing metabolic needs of the EPI as it transitions from the naive to the primed pluripotent state.[38] As such, we hypothesized that Hnf1b deficiency may result in aberrant nutrient transporter expression that would hamper the nutrient transfer to the EPI, which is required for the massive proliferation between E5.0 and E5.5. To examine this possibility, we determined module scores for various families of membrane transporters. We found a downregulation of Lipid, Ion, and Active Transmembrane transport, while protein transport remained upregulated more closely to E4.5 levels (Figure 7D). Focusing on lipid metabolism, recently reported to be essential for peri-implantation epiblast survival,[38] we found that two regulators of lipid metabolism, ApoA1 and ApoB were amongst the most differentially expressed genes of *Hnf1b*$^{-/-}$ embryos exhibiting significant downregulation compared to WT (Table S3 and Figures 7E and 7F). Since the solute carrier family of transporters (SLCs) is highly dysregulated in Hnf1b mutations in other tissues,[35] we next focused on SLC expression. The majority of SLCs expressed at this developmental stage were differentially expressed between Hnf1b$^{-/-}$ and WT (Figures 7G, 7H, and S13A–S13M) including the glucose transporter Slc2a1 (Figure 7G). Furthermore, we also observed severe downregulation of pyruvate dehydrogenase (Pdk1) (Figure S13N), another member of glucose metabolism. This led us to hypothesize that the impaired enrichment of glucose transport could contribute to the lethality observed in Hnf1b KO. To test whether this might be the case, we carried out a glucose uptake assay by incubating E5.0 WT and Hnf1b$^{-/-}$ embryos with the glucose analogue 2-NBDG.[39] Strikingly, we found that Hnf1b$^{-/-}$ embryos failed to take up glucose, while WT displayed large droplets (Figure 7I). Taken together, these results suggest that PE differentiation into the VE could be required to upregulate a set of nutrient transporters that may be necessary to provide the EPI with

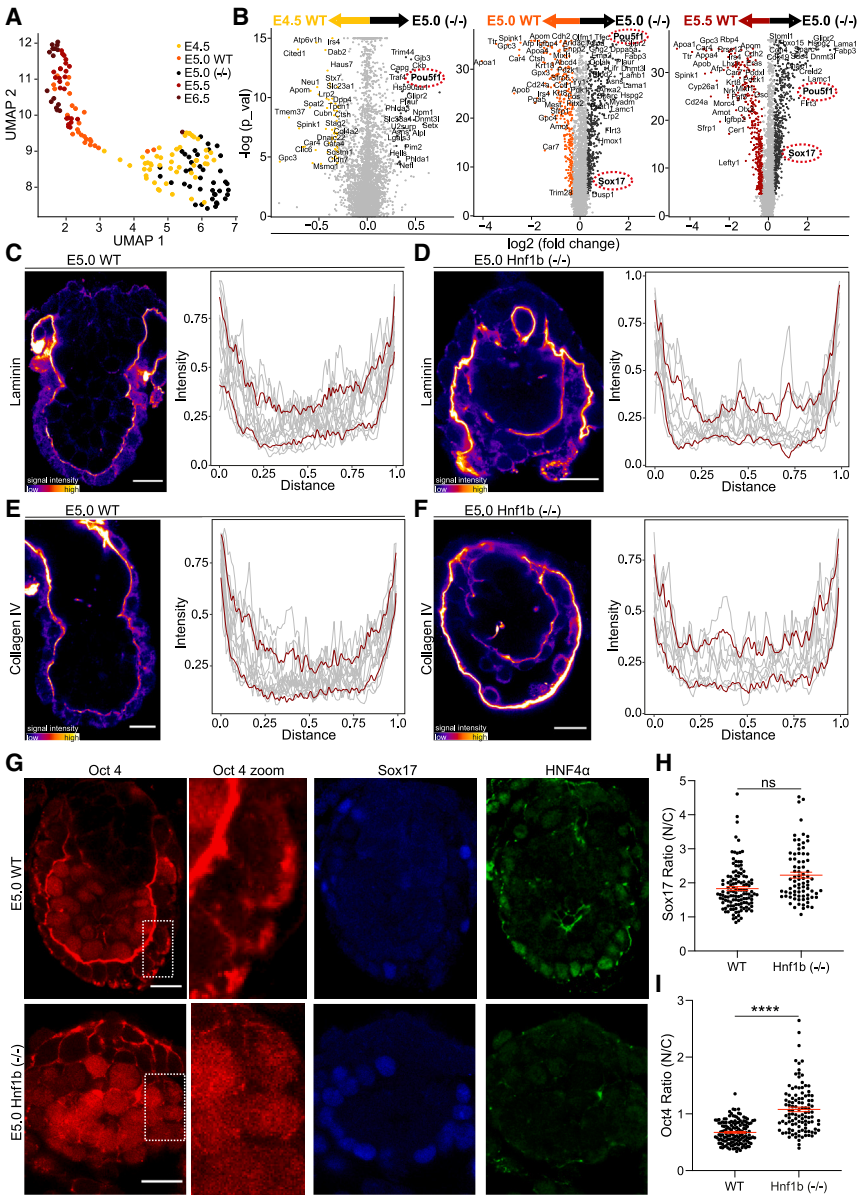

Figure 6. Hnf1b KO embryos exhibit distinct gene expression patterns for Hnf1b deficient embryos

(A) UMAP of WT primitive/visceral endoderm from E4.5-E5.5 and E5.0 Hnf1b KO embryos. E4.5 yellow, E5.0 WT orange, E5.5 pink, E6.5 red, E5.0 KO green.

(B) Volcano plots of differentially expressed genes of E4.5 (left), E5.0 WT (middle) and E5.5 (right) with E5.0 KO. Complete set of genes found in Tables S3C and S3D. (C and D) Assessment of Lama1 protein levels at E5.0 in WT (C) versus KO (D). left: Staining of Lama1, right: normalized intensity profile of laminin basement membrane, gray: individual plot profiles, red: ±SEM.

(E and F) Assessment of Collagen IV protein levels at E5.0 in WT (E) versus KO (F). left: Staining of Collagen IV, right: Normalized intensity profile of laminin basement membrane, gray: individual plot profiles Collagen IV WT n = 13, KO n = 8, Lama1 WT n = 13, KO n = 10 embryos, red: ±SEM. (G) Staining of E5.0 mutant embryos WT (top row) versus KO (bottom row). Oct4 (red), Sox17 (blue), Hnf4a (green).

(H) Quantitative analysis of normalized Sox17 levels in primitive/visceral endoderm (nuclear/cytoplasmic ratio) at E5.0 in WT vs. KO. Scatterplot, mean ± SEM, WT n = 9, KO n = 8 embryos, Analysis: nested t-test. WT-KO: p = 0.1109.

(I) Quantitative analysis of normalized Oct4 levels in primitive/visceral endoderm (nuclear/cytoplasmic ratio) at E5.0 in WT vs. KO. Scatterplot, mean ± SEM, WT n = 14, KO n = 11 embryos, Analysis: nested t-test. WT-KO: $p < 0.0001$. All Scale bars 20 μ m.

nutrients to allow its growth and expansion from E5.0 onwards (Figure 7J).

DISCUSSION

In this study, we investigated the differentiation of the PE into the VE and its role in embryo survival post-implantation. For this, we carried out a scRNAseq analysis of implanting embryos at E5.0, which we integrated with a published dataset for E4.5 and E5.5/E6.5.[27] Differential gene expression analysis showed that E5.0 endoderm represents an intermediate state between PE and VE, similar to the state of formative pluripotency between naive and primed pluripotency in the EPI.[12,33] Detailed analysis of the transcription levels of PE and VE marker genes such as *Gata4*, *Gata6*, *Sox7*, *Sox17*, *Pdgfra*, *Otx2*, *Lefty1*, *Cer1*, *Ttr*, and *Hhex*, revealed that the E5.0 VE exhibits a transcriptome that shares marker gene expression of both states. Interestingly, while for most factors observed (Gata4/Gata6/Otx2/Lefty1/Cer1) the transcription levels were also reflected in the protein levels, Sox7 deviated from the transcriptome by showing a unique upregulation of Sox7 protein at E5.0, while Sox17 instead showed severe downregulation at E5.0. Similarly, we found that the basement membrane protein levels did not match the continuous downregulation from E4.5 to E5.5 recorded at the transcriptome level. Instead, embryos at E5.0 exhibited low levels of Lama1 protein, compared to E4.5 and E5.5 embryos, which could be due to a transient upregulation of basement membrane degrading metalloproteinases (MMPs)[40] or a control of translation. Further research is required to fully understand the role of the transient fluctuations of these genes at the protein level. This intermediate endoderm state appears to present the switch point of Bmp activity in the maturating VE with the whole tissue concertedly activating Bmp signaling. Once universally activated in the VE, it becomes downregulated in the distal tip of the embryo, in line with the formation of the DVE.[30] Nodal

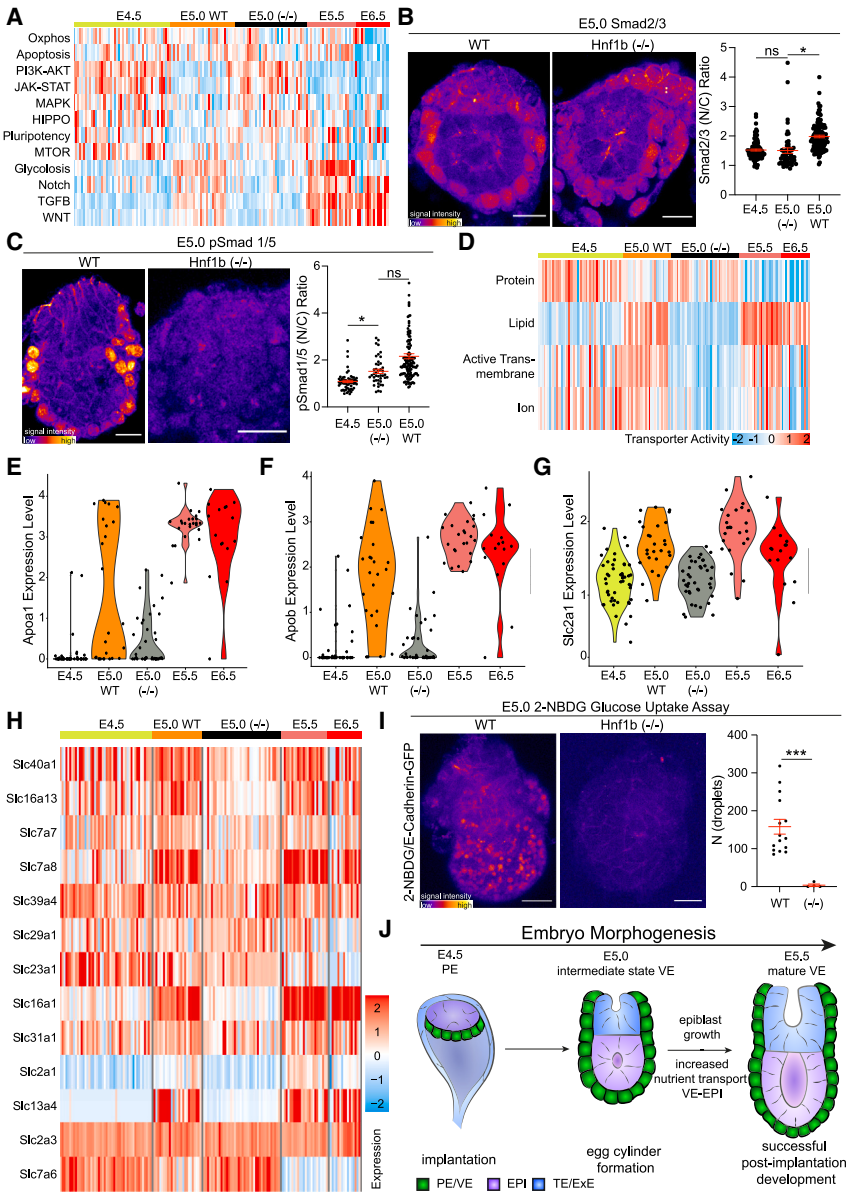

Figure 7. Hnf1b KO embryos fail to upregulate nutrient transport to support epiblast development

(A) Heatmap of KEGG signaling pathway enrichment in E4.5/E5.0WT/E5.0KO/E5.5/E6.5 primitive/visceral endoderm dataset. upregulation (red), downregulation (blue).

(B) Assessment of Nodal signaling in KO embryos. left: Staining of total Smad2/3 in E5.0 WT and KO embryos. right: Quantitative analysis of nuclear/cytoplasmic ratio in primitive/visceral endoderm E4.5 n = 13, E5.0KO n = 5, E5.0WT n = 13 embryos. Scatterplot, mean ± SEM, Analysis: nested t-test. E4.5-E5.0KO: p = 0.9719, E5.0KO-E5.0WT: p = 0.0449.

(C) Assessment of canonical Bmp signaling in KO embryos. left: Staining of pSmad1/5 in E5.0 WT and KO embryos. right: Quantitative analysis of normalized nuclear pSmad1/5 in primitive/visceral endoderm E4.5 n = 11, E5.0KO n = 5, E5.0WT n = 18 embryos. Scatterplot, mean ± SEM, Analysis: nested t-test. E4.5-E5.0KO: p = 0.0479, E5.0KO-E5.0WT: p = 0.2973.

(D) Heatmap of the enrichment of KEGG transporter terms for E4.5/E5.0WT/E5.0KO/E5.5/E6.5 primitive/visceral endoderm, KEGG terms indicated on the left. (E and F) Violin plots of Apoa1 (E), Apob (F) gene expression in E4.5/E5.0WT/E5.0KO/E5.5/E6.5 primitive/visceral endoderm.

(G) Violin plot of Slc2a1 gene expression in E4.5/E5.0WT/E5.0KO/E5.5/E6.5 primitive/visceral endoderm.

(H) Heatmap of normalized gene expression members of the SLC family of transporters for E4.5/E5.0WT/E5.0KO/E5.5/E6.5 primitive/visceral endoderm.

(I) Glucose uptake assay in WT versus KO embryos. 100 uM 2-NBDG treatment in E5.0 embryos for 15 min left: fire intensity staining of 2-NBDG/E-Cadherin-GFP in WT and KO embryo. Right: quantitative analysis of glucose droplet number in WT and KO embryos. WT n = 15, KO n = 4 embryos, 2 individual experiments. Scatterplot, mean ± SEM, Analysis: unpaired t-test: p = 0.0009.

(J) Final Model and Hypothesis: the primitive to visceral endoderm differentiation is required for epiblast growth and survival beyond E5.0.

signaling becomes even more strongly activated from E4.5 to E5.0, which then remains constant. Further analysis is required to understand the role of pERK in implanting embryos at E5.0, which we found active in a subset of embryos. Our results suggest that the PE to VE transition entails a transient, intermediate stage with a unique gene expression pattern and signaling activity.

To address the role of the PE to VE differentiation process for further development, we took advantage of an *Hnf1b* knockout embryo model, which has been shown to be lethal upon implantation due to failure of VE differentiation and egg cylinder formation.[23] We found that despite being delayed at E5.0, the *Hnf1b*$^{-/-}$ embryos were able to form egg cylinders, which however degenerated before reaching E5.5 explaining why this was not reported in the initial description of the *Hnf1b* knockout.[23,24] The initial EPI morphogenesis itself was not affected, as the EPI cells were able to exit from naive state of their pluripotency, polarize and form a lumen, showing that the differentiation of the VE is not required for this stage of EPI morphogenesis. However, the EPI in Hnf1b−/− embryos did not grow and eventually degenerated. Since cCasp3 imaging did not demonstrate a significant upregulation of apoptosis compared to WT embryos, it is likely that Hnf1b KO degeneration was due to a lack of cell proliferation. Through immunosurgical removal of the TE, we could confirm this lethality to be a result of a direct signaling interaction between the EPI and the PE/VE. When comparing the E5.0 KO VE with WT embryos, we saw differences in E-Cadherin levels pointing toward a defect

in epithelization. But when assessing apical-basal markers, Podxl and Itgb1, we found that these were correctly localized despite exhibiting lower intensity than controls. We hypothesize that their correct localization is sufficient to induce apical-basal polarity in the KO VE, but whether the lower protein expression has an added effect toward KO lethality will have to be investigated further. Similarly, when assessing Tgf β signaling pathways, BMP and Nodal, and FGF signaling activity, we recorded activity lying in-between E4.5 and E5.0 WT, which could not explain the lethal phenotype as it did not present a stark dysregulation. ScRNAseq of *Hnf1b*$^{-/-}$ embryos, showed that nutrient transporter pathways were severely dysregulated as found for Hnf1b KOs in other model systems.[35] We provide evidence that glucose uptake in the Hnf1b$^{-/-}$ PE/VE is diminished, which will result in severely downregulated glucose metabolism in the EPI. Genes associated with lipid metabolism were also impaired at a transcriptional level: Apob is one of the main regulators of lipid metabolism and was among the most differentially expressed genes between WT and *Hnf1b*$^{-/-}$ embryos, which suggests that a defect in lipid uptake and transport by the VE could result in EPI lethality following implantation. This possibility is supported by a recent study showing the requirement of lipid droplets during peri-implantation development.[38] *Apob* deficiency has been shown to be embryonic lethal[41] further supporting this hypothesis. Similarly, it has been shown that the dysregulation of members of the SLC transporter family results in severe congenital disorders.[35] Taken together, the sequencing data supported by the glucose uptake assay and the developmental defects reported for the components found downregulated in Hnf1b$^{-/-}$embryos, lead us to the hypothesis that the differentiation of the PE into the VE regulated by Hnf1b may be required to enable EPI growth and survival through the upregulation of nutrient transporters (Figure 7J). As human embryos show a similar expression pattern of Hnf1b and Hnf4a,[42] the role of the VE for EPI survival could be conserved across species.

Limitations of the study

Our study sheds light onto the understudied intermediate timepoint of E5.0 between the blastocyst (E4.5) and the mature egg cylinder (E5.5) and finds that the differentiation of the primitive to visceral endoderm is required for successful epiblast morphogenesis beyond E5.0. While we provide single cell sequencing data for E5.0, we do not provide data for E4.5 and E5.5. The lack of matched E4.5 and E5.5 VE RNA sequencing datasets within this study potentially raises the issue of technical variation influencing DE analysis between E5.0 and E4.5/E5.5. However, while the E5.0 visceral endoderm clusters in between the E4.5 and E5.5 visceral endoderm from the Argelaguet et al. dataset, other E5.0 lineages clustered closely with their more mature counterparts. Together, these findings suggest our analysis captures the biological differences between stages rather than technical variation. Future studies would benefit from the inclusion of E4.5 PE and E5.5 VE as well as greater numbers of cells from other E5.0 lineages.

We analyzed the activity of FGF and BMP signaling through the measurement of the nucelar-to-cytoplasmic ratio of pERK and pSmad1 respectively, which prevents the assessment of potential activity in cytoplasm or the cell membranes. For a full understanding of the signaling dynamics, live imaging of these transcription factors should be carried out.

RESOURCE AVAILABILITY

Lead contact

Requests for materials and further information should be directed to and will be fulfilled by the lead contact Dr Magdalena Zernicka-Goetz (mz205@cam.ac.uk).

Materials availability

This study did not generate any novel unique reagents.

Data and code availability

- The E5.0 WT and KO single-cell RNA-seq datasets generated in this study are available in the ArrayExpress repository: "E-MTAB-11140".
- Code used in this project is provided at https://github.com/dsiriwardena/Visceral-Endoderm-differentiation-is-mediated-by-Hnf1B-and-is-required-for-epiblast-survival.
- The original dataset of mouse immunofluorescence images and live imaging files are available upon reasonable request through the lead contact. Requests for additional, more detailed information or resources should be directed to and will be fulfilled by the lead contact Dr. Magdalena Zernicka-Goetz (mz205@cam.ac.uk).

ACKNOWLEDGMENTS

We thank C. Gantner and B. Weatherbee for critical feedback on the article, C. Ross for help in project conceptualization, feedback on the article and help with the immunosurgery experiments. This project has been made possible through the following grants to MZG: European Research Council (669198), the Wellcome Trust (207415/Z/17/Z), NIH Pioneer Award Fund (DP1 HD104575-01), Open Philanthropy/Silicon Valley Community Foundation. A.W. was supported by the EU Horizon 2020 Marie Sklodowska-Curie actions grant (ImageInLife, 721537) to M.Z.G. The T.B. lab is funded by the Wellcome Trust (WT RG89228) and the Centre for Trophoblast Research, University of Cambridge. T.B. is a WT-Royal Society Sir Henry Dale Fellow (WT RG89228).

AUTHOR CONTRIBUTIONS

A.W. and M.Z.G. conceived of and conceptualized the project with the help of N.C. A.W. designed and carried out all experiments and data analysis except single-cell sequencing. A.W. and D.S. collected embryos for single-cell sequencing. D.S. performed library preparation and together with C.P., bioinformatical analysis. A.W. wrote the article with the help of M.Z.G., D.S. and T.B. M.Z.G and T.B. supervised the project.

DECLARATION OF INTERESTS

The Authors declare no competing interests.

STAR★METHODS

Detailed methods are provided in the online version of this paper and include the following:

- KEY RESOURCES TABLE
- EXPERIMENTAL MODEL AND STUDY PARTICIPANT DETAILS
  - Mice
- METHOD DETAILS
  - Mouse embryo recovery and culture
  - Immunosurgery
  - Glucose uptake assay
  - Live imaging
  - Immunofluorescence staining and imaging

- Imaging, image processing and analysis
- Single cell sequencing

- QUANTIFICATION AND STATISTICAL ANALYSIS
  - Quantification and statistical analysis of the single cell sequencing data is described in the single cell sequencing chapter

SUPPLEMENTAL INFORMATION

Supplemental information can be found online at https://doi.org/10.1016/j.isci.2024.111671.

Received: February 9, 2022
Revised: July 30, 2023
Accepted: December 19, 2024
Published: December 23, 2024

REFERENCES

1. Molè, M.A., Weberling, A., and Zernicka-Goetz, M. (2020). Comparative analysis of human and mouse development: From zygote to pre-gastrulation. Curr. Top. Dev. Biol. *136*, 113–138. https://doi.org/10.1016/bs.ctdb.2019.10.002.
2. Smith, L.J. (1980). Embryonic axis orientation in the mouse and its correlation with blastocyst relationships to the uterus. Part 1. Relationships between 82 hours and 4 1/4 days. J. Embryol. Exp. Morphol. *55*, 257–277.
3. Copp, A.J. (1979). Interaction between inner cell mass and trophectoderm of the mouse blastocyst. II. The fate of the polar trophectoderm. J. Embryol. Exp. Morphol. *51*, 109–120.
4. Copp, A.J. (1978). Interaction between inner cell mass and trophectoderm of the mouse blastocyst. I. A study of cellular proliferation. J. Embryol. Exp. Morphol. *48*, 109–125.
5. Gardner, R.L., Papaioannou, V.E., and Barton, S.C. (1973). Origin of the ectoplacental cone and secondary giant cells in mouse blastocysts reconstituted from isolated trophoblast and inner cell mass. J. Embryol. Exp. Morphol. *30*, 561–572.
6. Papaioannou, V.E. (1982). Lineage analysis of inner cell mass and trophectoderm using microsurgically reconstituted mouse blastocysts. J. Embryol. Exp. Morphol. *68*, 199–209.
7. Weberling, A., and Zernicka-Goetz, M. (2021). Trophectoderm mechanics direct epiblast shape upon embryo implantation. Cell Rep. *34*, 108655. https://doi.org/10.1016/j.celrep.2020.108655.
8. Christodoulou, N., Weberling, A., Strathdee, D., Timpson, P., Zernicka-goetz, M., and Anderson, K.I. (2019). Morphogenesis of extra-embryonic tissues directs the remodelling of the mouse embryo at implantation. Nat. Commun. *10*, 3557. https://doi.org/10.1038/s41467-019-11482-5.
9. Bedzhov, I., and Zernicka-Goetz, M. (2014). Self-Organizing Properties of Mouse Pluripotent Cells Initiate Morphogenesis upon Implantation. Cell *156*, 1032–1044. https://doi.org/10.1016/j.cell.2014.01.023.
10. Wallingford, M.C., Angelo, J.R., and Mager, J. (2013). Morphogenetic analysis of peri-implantation development. Dev. Dynam. *242*, 1110–1120. https://doi.org/10.1002/dvdy.23991.
11. Smith, A. (2017). Formative pluripotency: the executive phase in a developmental continuum. Development *144*, 365–373. https://doi.org/10.1242/dev.142679.
12. Neagu, A., van Genderen, E., Escudero, I., Verwegen, L., Kurek, D., Lehmann, J., Stel, J., Dirks, R.A.M., van Mierlo, G., Maas, A., et al. (2020). In vitro capture and characterization of embryonic rosette-stage pluripotency between naive and primed states. Nat. Cell Biol. *22*, 534–545. https://doi.org/10.1038/s41556-020-0508-x.
13. Shahbazi, M.N., Scialdone, A., Skorupska, N., Weberling, A., Recher, G., Zhu, M., Jedrusik, A., Devito, L.G., Noli, L., Macaulay, I.C., et al. (2017). Pluripotent state transitions coordinate morphogenesis in mouse and human embryos. Nature *552*, 239–243. https://doi.org/10.1038/nature24675.
14. Stower, M.J., and Srinivas, S. (2014). Heading forwards: anterior visceral endoderm migration in patterning the mouse embryo. Philos. Trans. R. Soc. Lond. B Biol. Sci. *369*, 20130546. https://doi.org/10.1098/rstb.2013.0546.
15. Waldrip, W.R., Bikoff, E.K., Hoodless, P.A., Wrana, J.L., and Robertson, E.J. (1998). Smad2 Signaling in Extraembryonic Tissues Determines Anterior-Posterior Polarity of the Early Mouse Embryo. Cell *92*, 797–808. https://doi.org/10.1016/S0092-8674(00)81407-5.
16. Stower, M.J., and Srinivas, S. (2018). The Head's Tale: Anterior-Posterior Axis Formation in the Mouse Embryo. Curr. Top. Dev. Biol. *128*, 365–390. https://doi.org/10.1016/bs.ctdb.2017.11.003.
17. Perea-Gomez, A., Vella, F.D.J., Shawlot, W., Oulad-Abdelghani, M., Chazaud, C., Meno, C., Pfister, V., Chen, L., Robertson, E., Hamada, H., et al. (2002). Nodal antagonists in the anterior visceral endoderm prevent the formation of multiple primitive streaks. Dev. Cell *3*, 745–756.
18. Morris, S.A., Teo, R.T.Y., Li, H., Robson, P., Glover, D.M., and Zernicka-Goetz, M. (2010). Origin and formation of the first two distinct cell types of the inner cell mass in the mouse embryo. Proc. Natl. Acad. Sci. USA *107*, 6364–6369. https://doi.org/10.1073/pnas.0915063107.
19. Bassalert, C., Valverde-Estrella, L., and Chazaud, C. (2018). Primitive Endoderm Differentiation: From Specification to Epithelialization. Curr. Top. Dev. Biol. *128*, 81–104. https://doi.org/10.1016/bs.ctdb.2017.12.001.
20. Meilhac, S.M., Adams, R.J., Morris, S.A., Danckaert, A., Le Garrec, J.-F., and Zernicka-Goetz, M. (2009). Active cell movements coupled to positional induction are involved in lineage segregation in the mouse blastocyst. Dev. Biol. *331*, 210–221. https://doi.org/10.1016/j.ydbio.2009.04.036.
21. Plusa, B., Piliszek, A., Frankenberg, S., Artus, J., and Hadjantonakis, A.-K. (2008). Distinct sequential cell behaviours direct primitive endoderm formation in the mouse blastocyst. Development *135*, 3081–3091. https://doi.org/10.1242/dev.021519.
22. Srinivas, S., Rodriguez, T., Clements, M., Smith, J.C., and Beddington, R.S.P. (2004). Active cell migration drives the unilateral movements of the anterior visceral endoderm. Development *131*, 1157–1164. https://doi.org/10.1242/dev.01005.
23. Barbacci, E., Reber, M., Ott, M.O., Breillat, C., Huetz, F., and Cereghini, S. (1999). Variant hepatocyte nuclear factor 1 is required for visceral endoderm specification. Development *126*, 4795–4805.
24. Coffinier, C., Thépot, D., Babinet, C., Yaniv, M., and Barra, J. (1999). Essential role for the homeoprotein vHNF1/HNF1beta in visceral endoderm differentiation. Development *126*, 4785–4794.
25. Lau, H.H., Ng, N.H.J., Loo, L.S.W., Jasmen, J.B., and Teo, A.K.K. (2018). The molecular functions of hepatocyte nuclear factors – In and beyond the liver. J. Hepatol. *68*, 1033–1048. https://doi.org/10.1016/j.jhep.2017.11.026.
26. Chen, W.S., Manova, K., Weinstein, D.C., Duncan, S.A., Plump, A.S., Prezioso, V.R., Bachvarova, R.F., and Darnell, J.E. (1994). Disruption of the HNF-4 gene, expressed in visceral endoderm, leads to cell death in embryonic ectoderm and impaired gastrulation of mouse embryos. Genes Dev. *8*, 2466–2477. https://doi.org/10.1101/gad.8.20.2466.
27. Argelaguet, R., Clark, S.J., Mohammed, H., Stapel, L.C., Krueger, C., Kapourani, C.-A., Imaz-Rosshandler, I., Lohoff, T., Xiang, Y., Hanna, C.W., et al. (2019). Multi-omics profiling of mouse gastrulation at single-cell resolution. Nature *576*, 487–491. https://doi.org/10.1038/s41586-019-1825-8.
28. Nowotschin, S., Setty, M., Kuo, Y.-Y., Liu, V., Garg, V., Sharma, R., Simon, C.S., Saiz, N., Gardner, R., Boutet, S.C., et al. (2019). The emergent landscape of the mouse gut endoderm at single-cell resolution. Nature *569*, 361–367. https://doi.org/10.1038/s41586-019-1127-1.
29. Kyprianou, C., Christodoulou, N., Hamilton, R.S., Nahaboo, W., Boomgaard, D.S., Amadei, G., Migeotte, I., and Zernicka-Goetz, M. (2020).

Basement membrane remodelling regulates mouse embryogenesis. Nature *582*, 253–258. https://doi.org/10.1038/s41586-020-2264-2.

30. Yamamoto, M., Beppu, H., Takaoka, K., Meno, C., Li, E., Miyazono, K., and Hamada, H. (2009). Antagonism between Smad1 and Smad2 signaling determines the site of distal visceral endoderm formation in the mouse embryo. J. Cell Biol. *184*, 323–334. https://doi.org/10.1083/jcb.200808044.
31. Desgrange, A., Heliot, C., Skovorodkin, I., Akram, S.U., Heikkilä, J., Ronkainen, V.-P., Miinalainen, I., Vainio, S.J., and Cereghini, S. (2017). HNF1B controls epithelial organization and cell polarity during ureteric bud branching and collecting duct morphogenesis. Development *144*, 4704–4719. https://doi.org/10.1242/dev.154336.
32. Acampora, D., Omodei, D., Petrosino, G., Garofalo, A., Savarese, M., Nigro, V., Di Giovannantonio, L.G., Mercadante, V., and Simeone, A. (2016). Loss of the Otx2-Binding Site in the Nanog Promoter Affects the Integrity of Embryonic Stem Cell Subtypes and Specification of Inner Cell Mass-Derived Epiblast. Cell Rep. *15*, 2651–2664. https://doi.org/10.1016/j.celrep.2016.05.041.
33. Nichols, J., and Smith, A. (2009). Naive and Primed Pluripotent States. Cell Stem Cell *4*, 487–492. https://doi.org/10.1016/j.stem.2009.05.015.
34. Artus, J., Piliszek, A., and Hadjantonakis, A.-K. (2011). The primitive endoderm lineage of the mouse blastocyst: Sequential transcription factor activation and regulation of differentiation by Sox17. Dev. Biol. *350*, 393–404. https://doi.org/10.1016/j.ydbio.2010.12.007.
35. Niborski, L.L., Paces-Fessy, M., Ricci, P., Bourgeois, A., Magalhães, P., Kuzma-Kuzniarska, M., Lesaulnier, C., Reczko, M., Declercq, E., Zürbig, P., et al. (2021). Hnf1b haploinsufficiency differentially affects developmental target genes in a new renal cysts and diabetes mouse model. Dis. Model. Mech. *14*, dmm047498. https://doi.org/10.1242/dmm.047498.
36. Ferrè, S., and Igarashi, P. (2019). New insights into the role of HNF-1β in kidney (patho)physiology. Pediatr. Nephrol. *34*, 1325–1335. https://doi.org/10.1007/s00467-018-3990-7.
37. Wu, H., Yu, W., Meng, F., Mi, J., Peng, J., Liu, J., Zhang, X., Hai, C., and Wang, X. (2017). Polychlorinated biphenyls-153 induces metabolic dysfunction through activation of ROS/NF-κB signaling via downregulation of HNF1b. Redox Biol. *12*, 300–310. https://doi.org/10.1016/j.redox.2017.02.026.
38. Mau, K.H.T., Karimlou, D., Barneda, D., Brochard, V., Royer, C., Leeke, B., de Souza, R.A., Pailles, M., Percharde, M., Srinivas, S., et al. (2022). Dynamic enlargement and mobilization of lipid droplets in pluripotent cells coordinate morphogenesis during mouse peri-implantation development. Nat. Commun. *13*, 3861. https://doi.org/10.1038/s41467-022-31323-2.
39. Zou, C., Wang, Y., and Shen, Z. (2005). 2-NBDG as a fluorescent indicator for direct glucose uptake measurement. J. Biochem. Biophys. Methods *64*, 207–215. https://doi.org/10.1016/j.jbbm.2005.08.001.
40. Lu, P., Takai, K., Weaver, V.M., and Werb, Z. (2011). Extracellular Matrix Degradation and Remodeling in Development and Disease. Cold Spring Harbor Perspect. Biol. *3*, a005058. https://doi.org/10.1101/cshperspect.a005058.
41. Farese, R.V., Ruland, S.L., Flynn, L.M., Stokowski, R.P., and Young, S.G. (1995). Knockout of the mouse apolipoprotein B gene results in embryonic lethality in homozygotes and protection against diet-induced hypercholesterolemia in heterozygotes. Proc. Natl. Acad. Sci. USA *92*, 1774–1778. https://doi.org/10.1073/pnas.92.5.1774.
42. Molè, M.A., Coorens, T.H.H., Shahbazi, M.N., Weberling, A., Weatherbee, B.A.T., Gantner, C.W., Sancho-Serra, C., Richardson, L., Drinkwater, A., Syed, N., et al. (2021). A single cell characterisation of human embryogenesis identifies pluripotency transitions and putative anterior hypoblast centre. Nat. Commun. *12*, 3675. https://doi.org/10.1038/s41467-021-23758-w.
43. Picelli, S., Faridani, O.R., Björklund, A.K., Winberg, G., Sagasser, S., and Sandberg, R. (2014). Full-length RNA-seq from single cells using Smart-seq2. Nat. Protoc. *9*, 171–181. https://doi.org/10.1038/nprot.2014.006.
44. Liao, Y., Smyth, G.K., and Shi, W. (2014). featureCounts: an efficient general purpose program for assigning sequence reads to genomic features. Bioinformatics *30*, 923–930. https://doi.org/10.1093/bioinformatics/btt656.
45. Butler, A., Hoffman, P., Smibert, P., Papalexi, E., and Satija, R. (2018). Integrating single-cell transcriptomic data across different conditions, technologies, and species. Nat. Biotechnol. *36*, 411–420. https://doi.org/10.1038/nbt.4096.
46. Stuart, T., Butler, A., Hoffman, P., Hafemeister, C., Papalexi, E., Mauck, W.M., Hao, Y., Stoeckius, M., Smibert, P., and Satija, R. (2019). Comprehensive Integration of Single-Cell Data. Cell *177*, 1888–1902.e21. https://doi.org/10.1016/j.cell.2019.05.031.
47. Ma, H., Zhai, J., Wan, H., Jiang, X., Wang, X., Wang, L., Xiang, Y., He, X., Zhao, Z.-A., Zhao, B., et al. (2019). In vitro culture of cynomolgus monkey embryos beyond early gastrulation. Science *366*, eaax7890. https://doi.org/10.1126/science.aax7890.
48. Macaulay, I.C., Teng, M.J., Haerty, W., Kumar, P., Ponting, C.P., and Voet, T. (2016). Separation and parallel sequencing of the genomes and transcriptomes of single cells using G&T-seq. Nat. Protoc. *11*, 2081–2103. https://doi.org/10.1038/nprot.2016.138.
49. Martin, M. (2011). Cutadapt removes adapter sequences from high-throughput sequencing reads. EMBnet. J. *17*, 10–12. https://doi.org/10.14806/ej.17.1.200.
50. Dobin, A., Davis, C.A., Schlesinger, F., Drenkow, J., Zaleski, C., Jha, S., Batut, P., Chaisson, M., and Gingeras, T.R. (2013). STAR: ultrafast universal RNA-seq aligner. Bioinformatics *29*, 15–21. https://doi.org/10.1093/bioinformatics/bts635.

STAR★METHODS

KEY RESOURCES TABLE

REAGENT or RESOURCE	SOURCE	IDENTIFIER
Antibodies		
HNF4-alpha	Abcam	ab201460; RRID: AB_2927380
Gata6	R&D Systems	AF1700; RRID: AB_2108901
Laminin (lama1)	Sigma Aldrich	L9393; RRID: AB_477163
pErK	Cell Signaling Technology	4377T; RRID: AB_331775
p-Smad1/5	Cell Signaling Technology	9516S; RRID: AB_491015
Smad2/3	Cell Signaling Technology	8685S; RRID: AB_10889933
Cdx2	Biogenex	MU392-UC; RRID: AB_2335627
E-Cadherin	Thermo Fisher Scientific	13-1900; RRID: AB_86571
Integrin b1	Millipore	MAB1997; RRID: AB_2128202
PodxI	R&D Systems	MAB1556; RRID: AB_2166010
GM130	BD Bioscience	610822; RRID: AB_398141
Nanog	Abcam	ab80892; RRID: AB_2150114
Otx2	R&D Systems	AF1979; RRID: AB_2157172
Collagen IV	Millipore	AB769; RRID: AB_92262
Oct3/4	Santa Cruz	sc-5279; RRID: AB_628051
Sox17	R&D Systems	AF1924; RRID: AB_355060
AF 488 Donkey-*anti*-Rat	Life Technologies	A21208; RRID: AB_141709
AF 488 Donkey-*anti*-Rabbit	Thermo Fisher Scientific	A21206; RRID: AB_2535792
AF 568 Donkey-Anti-Rabbit	Life Technologies	A10042; RRID: AB_2534017
AF 568 Donkey-Anti Goat	Life Technologies	A11057; RRID: AB_2534104
AF 568 Donkey-*anti*-Mouse	Life Technologies	A10037; RRID: AB_2534013
AF 594 Donkey-*anti*-Rat	Thermo Fisher Scientific	A21209; RRID: AB_2535795
AF 647 Donkey-*anti*-Rabbi	Life Technologies	A-31573; RRID: AB_2536183
AF 647 Donkey-*anti*-Goat	Invitrogen	A21447; RRID: AB_141844
Phalloidin - Alexa Fluor 405	Thermo Fisher Scientific	A30104
Phalloidin - Alexa Fluor 488	Thermo Fisher Scientific	A12379
Phalloidin - Alexa Fluor 594	Thermo Fisher Scientific	A12381
DAPI	Thermo Fisher Scientific	D3571
Chemicals, peptides, and recombinant proteins		
DirectLysis Reagent	Viagen Biotech	301-C
Proteinase K	Qiagen	19131
CMRL	Thermo Fisher Scientific	11530037
CMRL-1066	Pan-Biotech	P04-84600
B27	Thermo Fisher Scientific	17504001
N2	Homemade Thermo Fisher Scientific	N/A 17502048
Penicillin-Streptomycin	Thermo Fisher Scientific	15140122
GlutaMAX	Thermo Fisher Scientific	35050038
Sodium Pyruvate	Thermo Fisher Scientific	11360039
Essential amino acids	Thermo Fisher Scientific	11130036
Non-essential amino acids	Thermo Fisher Scientific	11140035
Glucose	Sigma Aldrich	G8644
Fetal Bovine Serum	Stem Cell Institute, Cambridge	N/A
Anti-mouse-serum	Sigma Aldrich	M5774

(*Continued on next page*)

Continued

REAGENT or RESOURCE	SOURCE	IDENTIFIER
Rat serum	Home made, Boroviak Lab	N/A
Mineral Oil	Biocare Europe SRL	9305
2-NBDG	Gift from Elanor Minogue, Randall Johnson lab, Cambridge	
Caspase 3/7 Green Detection reagent	Thermo Fisher Scientific	C10723
Dynabeads Streptavidin C1	Invitrogen	65001
RNAsin	Promega	N2615
MgCl2	Invitrogen	AM9530G
Betaine	Sigma Aldrich	107-43-7
DTT	Invitrogen	R0861
dNTPs	Roche	50-196-5273
KAPA HiFi HotStart Readymix	Kapa	KK2601
AMPure XP beads	Beckman Coulter	A63881
Elution buffer	Qiagen	19086
RLT buffer	Qiagen	1053393
Critical commercial assays		
High Sensitivity DNA Analysis Kit	Agilent	5067–4626
Superscript II	Invitrogen	18064014
Bioanalyser high sensitivity chip system	Agilent	5067–4626
theNextera XT DNA kit	Illumina	FC-131-2001
Illumina HiSeq4000 (150bp read length)	Illumina	
Deposited data		
Single Cell RNA Sequencing E5.0 WT and Hnf1b−/− mouse embryos	This paper	Array Express: E-MTAB-11140
Single Cell RNA sequencing analysis code	This Paper	https://github.com/dsiriwardena/Visceral-Endoderm-differentiation-is-mediated-by-Hnf1B-and-is-required-for-epiblast-survival
Single Cell Sequencing Dataset of E4.5 and E5.5 mouse embryos	Argelaguet et al.[27]	
Experimental models: Organisms/strains		
Mouse lines		
Black6	Charles River	
CD1	Charles River	
E-Cadherin-GFP homozygous line	Christodoulou et al.[8]	
Hnf1b −/+ line EM:07827(B6.129P2(D2)-Hnf1b^{tm1Sce}/Orl)	EMMA institution Orleans	
Oligonucleotides		
HNF1b1Co 5′ TGCATCTTGCCGAAAGCTGAG 3’	Barbacci et al.[23]	
HNF1b1mut 5′ CTCTTCGCTATTACGCCAGCTG 3’	Barbacci et al.[23]	
HNF1b1WT 5′ AGGAGTGTCATAGTCGTCGC 3’	Barbacci et al.[23]	
5′ GCCGCCGGGATCACT 3′	This paper	
5′ TCCCATGGTGCCACACG 3′	This paper	
5′ AGAAGCTGGCGGACATGTAC 3′	This paper	
5′ TCCCATGGTGCCACACG 3′	This paper	
TSO: 5′-AAGCAGTGGTATCAACGCAGAGTAC ATrGrG+G-3′	Picelli at al.[43]	
ISPCR oligo: 5′-AAGCAGTGGTATCAACGCA GAGT-3′	Picelli at al.[43]	

(*Continued on next page*)

Continued

REAGENT or RESOURCE	SOURCE	IDENTIFIER
Biotinylated oligo-dT30VN-tailed olidonucleotides: 5′–AAGCAGTGGTATCAACGCAGAGTACT30VN-3′	Picelli at al.[43]	
Software and algorithms		
Fiji	https://imagej.net/software/fiji/	N/A
Graphpad Prism 7	GraphPad	https://www.graphpad.com/scientific-software/prism/
R	https://www.R-project.org/	v4.1.1
TrimGalore!	https://github.com/FelixKrueger/TrimGalore	N/A
STAR aligner v2.5.4	https://github.com/alexdobin/STAR	v2.5.4
FeatureCounts v1.6.0	Liao et al.[44]	v1.6.0
Seurat v4.0.1	Butler et al.[45]; Stuart et al.[46]	v4.0.1

EXPERIMENTAL MODEL AND STUDY PARTICIPANT DETAILS

Mice

The mice used in this study were kept according to national and international guidelines in the animal facility. All experiments performed were regulated by the Animals (Scientific Procedures) Act 1986 Amendment Regulations 2012 in addition to ethical review by the University of Cambridge Animal Welfare and Ethical Review Body (AWERB). Mice were kept in a pathogen-free facility and housed in individually ventilated cages. All work has been licensed by the Home Office (License numbers 70/8864, PP3370287 (from Sep 10th 2021 onwards).

METHOD DETAILS

Mice were culled by cervical dislocation upon any identification of health concern. Males used in this study were between 6 and 11 months old, the females 6–9 weeks old. For experiments on WT embryos, CD1 females were crossed with CD1 or homozygous E-Cadherin-GFP males. The Hnf1b −/+[23] line was derived through IVF of oocytes of Black6 mice with EMMA strain EM:07827(B6.129P2(D2)-Hnf1b^{tm1Sce}/Orl) Sperm, that was bought from the EMMA institution in Orleans. The pups were genotyped through PCR performed on DNA extracted from ear clips using the following primers: HNF1b1Co 5′ TGCATCTTGCCGAAAGCTGAG 3', HNF1b1mut 5′ CTCTTCGCTATTACGCCAGCTG 3', HNF1b1WT 5′ AGGAGTGTCATAGTCGTCGC 3'. The PCR cycles were performed as follows: 3min 95°C, 35x cycles of (15 s 94°C, 15 s 60°C, 30 s 72°C), 5min 72°C final elongation. The PCR product was then run on a 2% agarose gel, WT allele found at 518 bp, the Knock-out allele found at 410 bp. An endogenous E-Cadherin-GFP homozygous allele was introduced into the Hnf1b (+/−) line to enable live imaging by crossing a Hnf1b (+/−) male with an endogenous E-Cadherin-GFP homozygous female.[8] This resulted in the line being Hnf1b (+/−) and E-Cadherin-GFP homozygous. For line propagation, an Hnf1b (+/−), endogenous E-Cadherin-GFP homozygous male was crossed with an endogenous E-Cadherin-GFP homozygous female. The E-Cadherin-GFP genotype was assessed using 2 PCRs, the first targeting the transgenic allele and the second targeting the wildtype allele 1) 5′-GCCGCCGGGATCACT and 5′-TCCCATGGTGCCACACG and 2) 5′-AGAAGCTGGCGGACATGTAC and 5′-TCCCATGGTGCCACACG. The PCR cycles were run as follows: 4min 94°C, 30x cycles of (20 s 94°C, 30 s 58°C, 40 s 72°C), 3min 72°C final elongation).

For experiments on Hnf1b (−/−) embryos, a heterozygous female was crossed with a heterozygous male. The genotype of mouse embryos was either assessed through genotyping or Immunofluorescence staining of the direct downstream target of Hnf1b, Hnf4a, as no antibody for Hnf1b was available. To genotype individual embryos, the DNA was extracted using 24μL DirectPCR Lysis Reagent (Viagen Biotech, 301-C) complemented with 1μL Proteinase K (Qiagen, 19131). DNA extraction was carried out for 20 h at 55°C and terminated through heat inactivation for 45 min at 85°C.

Mouse embryo recovery and culture

Peri-implantation embryos and early post-implantation embryos (E4.5-E5.5) were dissected from the uteri or deciduas respectively and fixed immediately or transferred to equilibrated Advanced IVC medium: CMRL (11530037, Thermo Fisher Scientific) supplemented with 1X B27 (17504001, Thermo Fisher Scientific), 1X N2 (homemade or commercial 17502048, Thermo Fisher Scientific), 1X penicillin–streptomycin (15140122, Thermo Fisher Scientific), 1X GlutaMAX (35050038, Thermo Fisher Scientific), 1X sodium pyruvate (11360039, Thermo Fisher Scientific), 1X essential amino acids (11130-036, Thermo Fisher Scientific), 1X non-essential amino acids (11140035, Thermo Fisher Scientific), 1.8 mM glucose (G8644, Sigma) and 30% Fetal Bovine Serum (FBS) (Stem Cell Institute). The medium is based on an improved mouse culture system.[47] Embryos were cultured at 37°C and 5% CO_2 in a humidified atmosphere.

Immunosurgery

For immunosurgery, mouse embryos were dissected at E4.5 from mouse uteri and then incubated for 20 min in advanced IVC medium (for this experiment used without FBS) supplemented with 20% of anti-mouse serum (Sigma-Aldrich, M5774, gift of Elena Coruio-Simon, Jenny Nichols lab) at 37°C. Then, embryos were washed 3x in advanced IVC and placed in advanced IVC medium supplemented with 20% complement (home-made rat serum, Boroviak lab) and incubated for another 20 min at 37°C. Following this incubation step, embryos were washed 3x in advanced IVC medium using a narrow pipet, which removed the trophectoderm lineage. Embryos were then placed in hanging drops, 2–2.5 μl of advanced IVC +FBS and cultured for 24h, then embryos were transferred in drops of medium covered with mineral oil (Biocare Europe SRL, 9305) and cultured for an additional 24h. next day, embryos were fixed and assessed through immunofluorescence staining.

Glucose uptake assay

E5.0 embryos were dissected and then incubated for 15min in 100μM of 2-NBDG (a gift from Eleanor Minogue, Randall Johnson lab) in pure CMRL-1066 (Pan-Biotech, P04-84600). Then, embryos were washed 3x in CMRL-1066 and imaged at a z-resolution of 2μm with 488nm excitation laser. Following imaging, the DNA was extracted from the embryos and genotyping was carried out.

Live imaging

For live imaging, embryos were placed in small drops of medium in a glass bottom dish (MatTek Corporation P35G-1.5-14-C) covered with mineral oil. Embryos were imaged at indicated time intervals on a Leia multiphoton SP8 microscope with a 25x water objective using a z-step size of 1 μm. For excitation, a 488 nm laser was used. To image apoptosis, the medium was supplemented with 2 μM of Caspase 3/7 Green Detection reagent (Thermo Fisher Scientific, C10723).

Immunofluorescence staining and imaging

Embryos were fixed in 4% paraformaldehyde (PFA) in phosphate buffered saline (PBS) immediately upon recovery and kept on ice until the recovery was completed, then embryos were incubated for 20 min at room temperature (RT). All steps were caried out in a 96-well plate, with each well being coated with 100% FBS to prohibit attachment of the embryos to the bottom or sides of the wells. Embryos stained for phosphorylated proteins were incubated for 15 min in 100% MeOH at −20°C and then subjected to permeabilization, for normal staining, the MeOH incubation was skipped. For permeabilization, embryos were incubated for 20 min at RT with permeabilization buffer (0.3% Triton X-100/0.1 M Glycin in PBS). Embryos were blocked in blocking solution (0.1% Tween 20, 10% FBS, 1% bovine serum albumin (BSA) in PBS) for 1h at RT. Primary antibodies were prepared in blocking solution and incubated at 4°C overnight. Following day, embryos were washed 3x in PBS supplemented with 0.1% Tween 20 (PBST). Then, embryos were incubated with secondary antibodies in blocking solution for 3h at RT in the dark or overnight at 4°C in the dark. Embryos were washed in PBST. **Primary antibodies used:** rabbit-HNF4a (abcam, ab201460, 1:2000), goat-Gata6 (AF1700, R&D, 1:200), rabbit-Laminin lama1 (L9393, Sigma Aldrich, 1:300), rabbit-pERK (4377T, Cell Signaling Technology, 1:200), rabbit-phospho-Smad1/5 (Cell Signaling Technology, 9516S, 1:200), rabbit-Smad2/3 (Cell Signaling Technology, 8685S, 1:200), mouse-Cdx2 (Biogenex, MU392-UC, 1:200), rat E-Cadherin (13–1900, Thermo-Fisher, 1:300), rat Integrin b1 (MAB1997, Millipore, 1:150), rat-PodxI (MAB1556, R&D Systems, 1:200), mouse-GM130 (610822, BD, 1:200), rabbit-Nanog (ab80892, Abcam, 1:200), goat-Otx2 (AF1979, R&D Systems, 1:200), goat-collagen IV (AB769, Millipore, 1:100), mouse-Oct3/4 (sc-5279, Santa Cruz, 1:200), goat-Sox17 (AF1924, R&D Systems, 1:400). **Secondary antibodies and stains used**: Phalloidin- Alexa Fluor (AF) 405 (A30104, Thermo Fisher Scientific 1:250), Phalloidin-AF 488 (A12379, Thermo Fisher Scientific, 1:500), Phalloidin-AF 594 (A12381, Thermo Fisher Scientific, 1:250), DAPI (D3571, Thermo Fisher Scientific, 1:500), AF 488 Donkey-*anti*-Rat (A-21208, Life Technologies, 1:500), AF 488 Donkey-*anti*-Rabbit (A21206, Thermo Fisher Scientific, 1:500), AF 568 Donkey-Anti-Rabbit (A10042, Life Technologies, 1:500), AF 568 Donkey-Anti Goat (A-11057, Life Technologies), AF 568 Donkey-*anti*-Mouse (A10037, Life Technologies, 1:500), AF 594 Donkey-*anti*-Rat (A21209, Thermo Fisher Scientific, 1:500), AF 647 Donkey-*anti*-Rabbit (A-31573, Life Technologies, 1:500), AF 647 Donkey-*anti*-Goat (A21447, Invitrogen, 1:500).

Imaging, image processing and analysis

Embryos were imaged using a Leica multiphoton SP8 microscope with a 63x oil objective. E5.5 and E6.5 embryos were imaged using a 40x oil objective. Z-stacks were taken at a z-step size of 0.6 μm. The images were processed and analyzed using the open source Fiji software.

In single-channel images as well as stills from live imaging, the fire-LUT of Fiji was chosen. This LUT ranges from yellow-white to dark purple-black to indicate high to low signal intensity. This visualisation provides an additional level of information on signal intensity compared with common single-coloured channels. Color bars are provided in each panel. A full explanation of the fire LUT is provided by ImageJ.net: (https://imagej.net/ij/plugins/lut-editor.html).

Single cell sequencing

Sample preparation

Following dissection and Reichert's membrane removal, which included removal of the mural trophectoderm and the Parietal Endoderm, E5.0 embryos were dissociated in 0.25% Trypsin-EDTA (Cambridge Stem Cell institute) for 15 min at 37C and pipetted

vigorously to obtain a single cell suspension in normal culture media. Single cells were picked by mouth pipette using a blunted microcapillary with internal diameter 15 μM and under a dissection microscope. In total, 151 cells were collected from 6 mouse embryos. Cells were collected into 0.2 mL tubes with 4 μL lysis buffer and immediately snap frozen on dry ice. Smart-seq2 library preparation was carried out in 96W format as previously described.[43] Library quality was assessed using the High Sensitivity DNA Analysis Kit (5067-4626, Agilent) on the 2100 Bioanalyzer system (Agilent).

Library preparation

For transcriptome libraries (modified protocol of[48]), complementary DNA (cDNA) was synthesised by reverse transcription using Superscript II (Invitrogen, 200 U/ul) and template-switching oligos (TSO; Exiqon, 100 μM) in 5x Superscript II first strand buffer (Invitrogen) containing RNAse-inhibitor (Promega, 1U/ul), MgCl2 (Invitrogen, 1M), Betaine (Sigma, 5M), DTT (Invitrogen, 100 mM) and dNTPs (Roche, 10mM). Subsequently, material was amplified by PCR using the KAPA HiFi HotStart Readymix (KK2601, Kapa) and IS PCR primers (IDT, 10 uM). Sample clean-up was performed with AMPure XP beads (A63881, Beckman Coulter) at RT, using 80% ethanol, and cDNA samples were eluted in 20 μl elution buffer (Qiagen). For quality control, the DNA concentration of eleven randomly chosen samples per plate was measured using the Agilent Bioanalyser high sensitivity chip system (5067-4626, Agilent Technologies) according to the manufacturer's protocol. Following successful quality control indicated by cDNA between 0.5 and 3 kb, tagmentation reaction was performed using theNextera XT DNA kit (FC-131-2001, Illumina). Samples were indexed using the Nextera XT 96-index kit (Illumina) and adapter-ligated fragments were amplified using the Nextera PCR master mix according to the manufacturer's instructions. According to their quality, measured by the Bioanalyzer, samples volumes equivalent to a concentration in the range of 200-500pg were collected and pooled. Following a two-step library purification of the pooled samples with Ampure XP beads and 80% ethanol solution at RT (1:0.5 ratio and 1:0.2 ratio of beads to original volume), cDNA was eluted in 22 μL elution buffer and quality control was performed using the Bioanalyzer. Pooled libraries were sequenced on an Illumina HiSeq4000 platform with a read length of PE 150 bp. The single cell transcriptomes were merged with the combined public dataset without batch corrections.

QUANTIFICATION AND STATISTICAL ANALYSIS

For all statistical analysis concerning Immunofluorescence images, GraphPad Prism 9 was used. The sample size for the different experiments is based on previous experimental experience. Each experiment was carried out at least 3 times, meaning for WT stainings that embryos were collected at 3 different dates. Each quantification is shown as a point cloud with Mean ± SEM, the *p*-values and n-numbers are given in the figure legend.

Intensity measurements: For nuclear to cytoplasmic ratio and normalised nuclear expression level assessment, the plane with the maximum size of the nucleus was selected, nucleus and cytoplasm encircled and the mean gray value taken for 3 planes. The average nuclear to cytoplasmic ratio then plotted with one dot representing a single cell. For E-Cadherin intensity assessment, the mean gray value of the VE cell-cell adhesions was normalised against the average mean gray value of the VE-epiblast cell-cell adhesions and then plotted with every dot representing a single cell. For Itgb1 analysis, the basal side was normalised against the apical surface of the VE cells. Each datapoint represents a single cell. For PodxI analysis, the apical surface of the VE cells was normalised against the basal side of the VE cells, each datapoint represents a single cell. The Laminin and Collagen intensity profiles were obtained in 3 planes, the average intensity values were overlayed and plotted.

Quantification and statistical analysis of the single cell sequencing data is described in the single cell sequencing chapter

Single cell sequencing bioinformatic analysis

Raw sequencing data was downloaded, trimmed of adapter sequences using TrimGalore![49] mapped to the UCSC mouse reference genome mm10 using STAR aligner v2.5.4.[50] Samples with more than 100,000 mapped reads and a mapping efficiency of more than 60% were used (Table S4). Gene counts were quantified using FeatureCounts v1.6.0.[44] Individual datasets were normalised using the NormalizeData function in the R package Seurat.[45]

E5.0 samples passing QC were analyzed using Seurat v4.0.1. Knock outs were determined by visualizing read alignment in the Hnf1b locus (Figure S14A). Principal component analysis was run using the inbuilt RunPCA function, with nonlinear dimensionality reduction techniques generated using RunUMAP. Dimensionality reduction was visualised in 2D using ggplot. Marker genes were identified using FindMarkers for cell or cluster specific comparisons or FindAllMarkers using a Wilcoxon Rank-Sum test (only positive, minimum percent 20%, log FC threshold 0.1). Lineage specific expression profiles for key marker genes were calculated using the AverageExpression function and visualised using ggplot or the DoHeatmap function. Lineage assignment was conducted by unbiased cluster generation using FindClusters followed by annotation via lineage marker expression. Ultimately, 39 knockout and 27 wild type VE cells were sequenced. Pathway enrichment was calculated using pathway annotations from KEGG and the AddModuleScore function. E5.0 data was merged with published datasets (GSE121650) using Canonical Correlation Analysis (CCA) and mutual nearest neighbor (MNN) approaches. Specifically, FindIntegrationAnchors was run using 4000 features and IntegrateData (with 20 dimensions) was used to calculate corrected gene expression matrices.